Eindhoven University of Technology

MASTER

Ultrafast manipulation of magnetism in a Van der Waals ferromagnet

van Kooten, S.C.P.

Award date:
2020

Link to publication

Disclaimer
This document contains a student thesis (bachelor's or master's), as authored by a student at Eindhoven University of Technology. Student theses are made available in the TU/e repository upon obtaining the required degree. The grade received is not published on the document as presented in the repository. The required complexity or quality of research of student theses may vary by program, and the required minimum study period may vary in duration.

General rights
Copyright and moral rights for the publications made accessible in the public portal are retained by the authors and/or other copyright owners and it is a condition of accessing publications that users recognise and abide by the legal requirements associated with these rights.

- Users may download and print one copy of any publication from the public portal for the purpose of private study or research.
- You may not further distribute the material or use it for any profit-making activity or commercial gain

Ultrafast manipulation of magnetism in a Van der Waals ferromagnet

S. C. P. van Kooten

March 6, 2020

Supervisors:
ir. T. Lichtenberg
ir. C. F. Schippers
dr. M. H. D. Guimarães
prof. dr. B. Koopmans

Physics of Nanostructures
Department of Applied Physics
Eindhoven University of Technology

Abstract

Van der Waals materials and ultrafast magnetization dynamics are both of interest in spintronic research and applications. This work bridges the gap between these fields by presenting the first observation of ultrafast demagnetization in a Van der Waals material. The measurements were conducted on Fe_3GeTe_2, a novel Van der Waals ferromagnet that exhibits an intrinsic, thickness-dependent transition from three to two-dimensional magnetism. The findings contribute to the field of Van der Waals spintronics by illustrating excitation and probing of ultrafast spin dynamics in a Van der Waals material. Moreover, being a complementary material, further studies on ultrafast demagnetization in Fe_3GeTe_2 can contribute to an increased fundamental understanding of the heavily debated microscopic origin(s) behind ultrafast demagnetization.

Bulk and thin Fe_3GeTe_2 were studied using static and time-resolved techniques. The bulk Curie temperature was measured as $191 \pm 2\,\mathrm{K}$, slightly below its literature value. Combining this result with energy dispersive X-ray spectroscopy on the bulk crystal indicates that this deviation is due to a (spatially varying) iron deficiency in the crystal. Thin Fe_3GeTe_2 was studied by measuring the ferromagnetic hysteresis of uniform magnetic domains. The measurements were performed with and without magnetic field-cooling, where it was found that field-cooling likely suppresses magnetic domain formation and therefore stabilizes magnetostatic behavior compared to the results obtained for cooling down without an applied field.

Time-resolved measurements were conducted to obtain the electron-phonon relaxation timescale τ_E and demagnetization timescale τ_M. Typical values at a temperature of 90 K with a laser fluence of $25.7\,\mu\mathrm{J\,cm^{-2}}$ yield $\tau_E = 0.20 \pm 0.01\,\mathrm{ps}$ and $\tau_M = 13.6 \pm 0.3\,\mathrm{ps}$. Their relative magnitude corresponds with the qualitative observation of type II magnetization dynamics, i.e. $\tau_E < \tau_M$. It is furthermore observed that the coupling between the spin dynamics and electron-phonon dynamics is relatively weak compared to other transition metals, as indicated by the relatively long magnetic timescale.

Finally, the characteristic timescales were measured as a function of temperature, for which the obtained result is well in correspondence with existent models. The microscopic three-temperature model was fitted to the obtained result, yielding the material-dependent constant $R = 0.085 \pm 0.005\,\mathrm{ps^{-1}}$. Comparing R to the electron-phonon relaxation rate close to the Curie temperature τ_{E0} yields $R \ll 1/\tau_{E0}$, indicating type II dynamics are intrinsic to FGT over a wide temperature and laser fluence range.

Overall, the results obtained in this work provide a solid basis for further investigations of ultrafast magnetism in Fe_3GeTe_2 and other Van der Waals materials.

Contents

List of abbreviations

2D	two-dimensional
3D	three-dimensional
3TM	three-temperature model
A	analyzer
BKT	Berezinskii-Kosterlitz-Thouless
BS	beam splitter
DL	delay line
EDX	energy dispersive X-ray spectroscopy
FC	field-cooling
FGT	Fe_3GeTe_2
FM	ferromagnetic
FWHM	full width at half maximum
LCP	left-hand circularly polarized
LIA	lock-in amplifier
M3TM	microscopic three-temperature model
MCB	magnetic circular birefringence
MCD	magnetic circular dichroism
MD	multi-domain
MFM	magnetic force microscopy
MOKE	magneto-optical Kerr effect
OOP	out-of-plane
P	polarizer
PD	photodetector
PEM	photoelastic modulator
PM	paramagnetic
PMA	perpendicular magnetic anisotropy
RCP	right-hand circularly polarized

SD	single-domain
SNR	signal-to-noise ratio
SO	spin-orbit
SEM	scanning electron microscopy
SEMPA	scanning electron microscopy with polarization analysis
SQUID	superconducting quantum interference device
STM	scanning tunneling microscopy
TR	time-resolved
VdW	Van der Waals
ZFC	zero-field-cooling

Chapter 1

Introduction

In 2004, work by Novoselov et al. about the electric field effect in graphene [1] solidified the basis for a completely new field in physics. In their work they describe the electric field effect in 'atomically thin layers of graphite' (which are referred to as graphene) and showed two major findings. First, they showed that micrometer sized, atomically flat layers of graphite can be fabricated by using only a simple piece of scotch tape. Moreover, their work also highlighted one of the, as became apparent later, many unique properties of graphene [2] and other layered materials [3], such as electrons appearing massless in graphene [4] and thickness-dependent behavior of the band structure in MoS_2 [5, 6]. In the years following their initial work, the combination of unique properties and accessible means of fabrication spiked interest in these materials. Already in 2009 several papers were appearing every day [7] and in 2010 the Nobel Prize in Physics was awarded to A. K. Geim and K. S. Novoselov for their efforts regarding graphene [8].

As the title of the earlier mentioned work already reveals, graphene is a single, atomically thin layer of graphite, belonging to the group of so-called 'Van der Waals (VdW) materials'. Such materials consist of two-dimensional (2D) crystalline planes of only one or a few atoms thick, stacked on top of each other by Van der Waals bonds. The inter-plane VdW bonds are relatively weak compared to the much stronger intra-plane bonds, which are typically of covalent or ionic origin. It is this difference in bonding strength that allows for efficient cleaving using scotch tape, resulting in monolayers of graphite or graphene.

Furthermore, due to the nature of the inter-plane VdW bonds, fundamental differences arise between (hetero)structures of stacked VdW planes and 'regular' epitaxial films. In contrast to covalent or ionic bonds, VdW bonds do not rely on any bonding mechanism between specific atoms or ions. Therefore, two-dimensional planes of VdW materials can be stacked on top of each other regardless of lattice matching and relative orientation [9, 10]. Additionally, the lack of dangling bonds[1] leaves the surfaces of VdW materials near-perfect, preventing the emergence of trap states due to surface defects between two adjoined materials, an often undesired complication in other types of heterostructures [9].

[1] Interfaces between two different crystals will often contain atoms with unsatisfied valence, i.e. not all their possible electronic bonds are satisfied. Those incomplete bonds are commonly referred to as dangling bonds.

Following the activity around graphene, and looking for opportunities to use graphene in VdW heterostructures, a search began for other VdW materials. Among them are for example the insulator hexagonal boron nitride (hBN) and the semiconductor molybdenum disulfide (MoS_2) [11]. The discoveries of these new materials led to new physics and applications [9, 10, 12, 13]. Some examples include advancements in superconduction and other many-body phenomena [13–15], strong thickness-dependent behavior of the electronic structure [5, 6] and the formation of superlattices by creating Moiré patterns[2] [16–18]. Furthermore, opportunities for VdW materials in spintronic applications have also been highlighted [19–21]. However, Van der Waals materials that are magnetic themselves have only recently come under attention [22–25]. This is in surprising contrast to the large amount of research performed in the field of (opto-)spintronics [26–30] and also to the extensive use of magnetic materials in everyday life devices.

A contributing factor to the lack of magnetic VdW materials can be found in the more fundamental limitations that arise in the search for new, usable VdW materials. In the first place, decreasing layer thickness generally leads to a decrease in melting temperature, limiting the amount of materials that retain their 2D character at room temperature. Furthermore, most bulk materials are encapsulated in a naturally formed protective layer, e.g. by oxidation of the outer layers. Evidently, the formation of such a layer is not desirable for surfaces of only one or few atoms thickness. In common epitaxial processes, materials and structures are therefore often grown in vacuum conditions and covered with a protective layer. While epitaxial growth of VdW materials has been demonstrated using molecular beam epitaxy and chemical vapor deposition [31], the quality of these methods does not (yet) match the quality of manual exfoliation via the scotch tape method [10, 31, 32]. As an alternative, a protective layer is often created by manual encapsulation in hBN [33, 34], although this approach is not scalable and often complicates the fabricating process by requiring fabrication under inert atmospheres.

Lastly, specifically in the case of magnetic materials another limitation arises. As follows from the Mermin-Wagner theorem [35, 36], order in continuously symmetric systems of two or less dimensions cannot arise spontaneously at finite temperatures. This means that in magnetic systems, no ordered magnetic phase exists in two or less dimensions if the magnetism follows a Heisenberg (or any other continuously symmetric) Hamiltonian. For an ordered phase to arise, it is necessary that an additional mechanism (e.g. anisotropy) is present to break the continuous (Heisenberg) symmetry [23]. For example, the well-known 2D Ising model [37] incorporates such symmetry breaking and indeed gives rise to the existence of an ordered phase.

1.1 Van der Waals ferromagnet Fe_3GeTe_2

Despite those limitations, several magnetic VdW materials have been discovered recently [23–25]. This work intends to further explore the magnetic properties of VdW materials, specifically by studying Fe_3GeTe_2 (FGT). FGT is a ferromagnetic (FM) metal where the magnetic moments are carried by the conduction

[2] A specific type of superlattice that is created by overlaying similar periodic 2D structures with a certain translational and/or rotational mismatch.

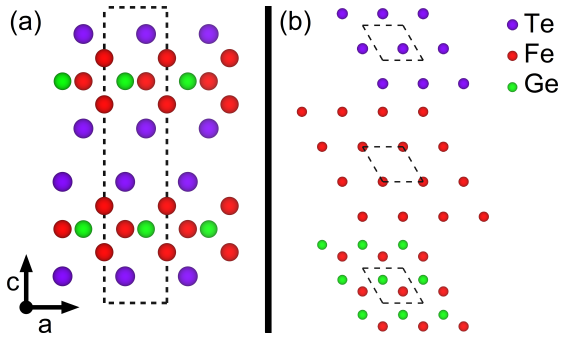

Figure 1.1: (a) Side view of the FGT crystal structure. To construct the bulk unit cell (denoted by the dashed box) at least two layers are required. (b) Top view of the three different triangular lattice planes that are present in a single layer of FGT. A full monolayer consists of five stacked planes in the order Te-Fe-Fe/Ge-Fe-Te. The unit cell is denoted by the dashed box.

electrons, i.e. the magnetism is itinerant, and the Curie temperature (T_C) is around $220-230$K [38–44]. A hard magnetic phase emerges for sufficiently thin layers of FGT [44, 45], meaning that a (substantial) non-zero magnetization persists after removal of an applied magnetic field.

Bulk FGT crystallizes in a layered hexagonal crystal structure of space group $P6_3/mmc$ [38] and its atomic structure is shown in Figure 1.1a. A single layer of FGT is approximately 0.8 nm thick [44] and consists of an iron-germanium lattice sandwiched between tellurium atoms. The bulk lattice is subsequently formed by stacking the planes in the c-direction through a VdW gap between the tellurium atoms. Finally, as follows from the space group symmetry, at least two layers are needed to form the bulk unit cell, as also indicated by the dashed box in Figure 1.1a.

Zooming in on a monolayer of FGT reveals that it is essentially formed by five two-dimensional triangular lattice planes stacked on top of each other (see Figure 1.1b). The central plane contains a first type of iron ions (Fe-I) which form a hexagonal lattice together with the germanium atoms. Located above and below this Fe-Ge plane are two identical triangular lattice planes formed by a second type of iron ions (Fe-II). Finally, this three-plane structure is sandwiched between two identical triangular lattice planes containing tellurium atoms. It is expected that the Fe-I ions are Fe^{2+} and the Fe-II ions are Fe^{3+} ions [38].

The magnetism in FGT follows from the exchange splitting of the Fe $3d$ orbitals at the Fermi level [40, 42], which is a common source of magnetism also found in other transition metal ferromagnets. In addition, FGT has strong magnetocrystalline anisotropy, with its easy axis along the c-direction and the hard axis in the ab-plane. In bulk FGT, this leads to the formation of opposing stripe domains with their magnetization along the c-axis [44, 46–48]. Eventually, if the thickness is decreased sufficiently (< 100nm), a hard, single-domain phase emerges with perpendicular magnetic anisotropy (PMA). The related thickness-temperature phase diagram is shown in Figure 1.2, indicating the single-domain (SD) FM phase, the multi-domain (MD) FM phase and the paramagnetic (PM) phase.

It is furthermore observed that as the thickness decreases below 4 nm, the

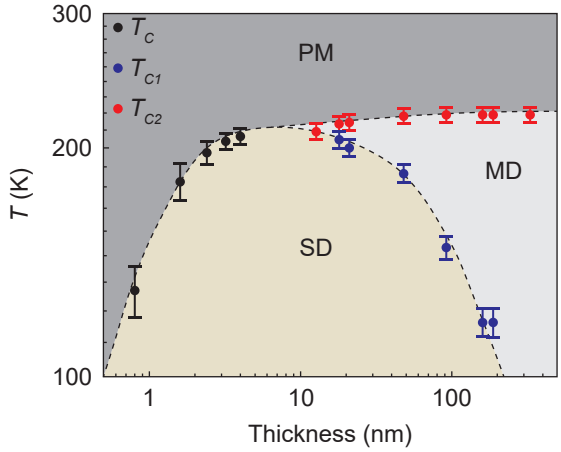

Figure 1.2: The magnetic phase diagram of FGT as a function of thickness and temperature T, indicating the single-domain (SD) and multi-domain (MD) ferromagnetic and paramagnetic (PM) phases as a function of thickness and temperature. *Adapted from [44].*

Curie temperature drops from its bulk value of $\sim 220\,\mathrm{K}$ to $\sim 130\,\mathrm{K}$. This drop is associated with a transition from three- to two-dimensional magnetism, yielding 3D bulk magnetism for 6 or more layers, a crossover phase for 2-5 layers and 2D Ising magnetism for single layer FGT [44]. This remarkable property makes FGT an interesting material for more general, fundamental studies on magnetism and spintronics, in addition to its potential use as a VdW ferromagnet.

Studies on the magnetic properties of FGT have mostly been limited to static measurements, such as measuring the magnetization as a function of applied field [41, 44, 45, 49]. In this work, the ultrafast, (sub-)picosecond magnetization dynamics of FGT are investigated using time-resolved pump-probe spectroscopy, which to the author's best knowledge also constitutes the first observation of ultrafast demagnetization in any magnetic VdW material.

1.2 Ultrafast magnetization dynamics

A femtosecond pump-probe scheme is used to both excite and probe the magnetization dynamics in FGT on ultrafast timescales. By using laser pulses with a pulse length in the range of tens of femtoseconds, a resolution well below 1 picosecond can be obtained for both exciting and probing the dynamics within FGT.

This scheme was successfully employed to measure ultrafast magnetization dynamics in nickel for the first time in 1996 by Beaurepaire et al. [50]. The timescales associated with this process were determined to be in the order of picoseconds or hundreds of femtoseconds [50–53], which was in remarkable contrast to earlier measurements and theoretical models for e.g. demagnetization processes in gadolinium [54, 55], with associated timescales in the order of 100 ps. In the following years, measurements were performed on other transition metal ferromagnets such as iron and cobalt, showing a similar results as in nickel [53].

On a phenomenological basis, the results were explained in terms of the so-called three-temperature model [50]. This model describes the thermodynamics of the demagnetization process in terms of three subsystems, the electron, spin and phonon (or lattice) subsystem, and their mutual interactions. However, this model lacks proper arguments for the microscopic origin behind the demagnetization process, does not account for conservation of angular momentum and lacks an explanation for the order of magnitude difference in timescales between rare-earth ferromagnets such as gadolinium, which have magnetic $4f$ orbitals, and transition metal ferromagnets such as iron, cobalt and nickel, which have magnetic $3d$ orbitals. Microscopic models can typically be divided into local [56] and non-local [57] approaches, but the exact mechanisms behind ultrafast demagnetization and their respective contributions remain subject of discussion until present day [27, 58–60].

Despite the discussion regarding its microscopic origin, significant experimental progress has been made since the initial discovery of ultrafast demagnetization in nickel, which has been developing towards device applications in recent years. Furthermore, so-called femtomagnetic processes are also highlighted for their potential use in spintronics [60, 61]. Examples of (recent) experimental progress include all-optical excitation and probing of spin waves [62], all-optical magnetic switching in ferrimagnetic alloys [63, 64], all-optical, polarization-dependent writing of ferromagnetic bits [65, 66] and the excitation of terahertz spin waves in ferromagnetic bilayers [67–69].

However, ultrafast demagnetization and its derived femtomagnetic processes have not been previously observed in Van der Waals materials, leaving a gap that will be filled by the results presented in this work. Furthermore, being a complementary material exhibiting ultrafast demagnetization, studies on FGT could also lead to more fundamental insight in the processes behind femtomagnetism, in particular due to its intrinsic transition from two- to three-dimensional magnetism.

1.3 This thesis

This work aims to combine femtomagnetism with Van der Waals materials, two topics that have been individually highlighted for their potential use in spintronics. To do so, the demagnetization of ferromagnetic Fe_3GeTe_2 is investigated using femtosecond pump-probe spectroscopy. Due to FGT being a transition metal ferromagnet, it proves a viable candidate for ultrafast demagnetization, as is confirmed by the results obtained in this work (see chapter 4).

To interpret the results, the necessary theoretical concepts regarding two-dimensional magnetism, magnetic ordering, phase transitions and femtomagnetism will be discussed and applied to FGT in the following chapter. Subsequently, the experimental methods used for sample preparation and qualification, and (time-resolved) magneto-optical measurements will be elaborated on. The obtained results and their interpretation will be discussed in chapter 4, including the main result regarding the first observation of ultrafast demagnetization in a Van der Waals material. Finally, a summary and conclusion of the work is given in chapter 5, including implications of the experimental findings and an outlook for future research regarding femtomagnetism in VdW materials.

Chapter 2

Theory

This chapter will discuss the relevant theoretical concepts regarding the experiments performed. At first, general concepts involving magnetic ordering, phase transitions and the influence of dimension on these mechanisms will be discussed, which is largely illustrated by using the Ising model as an example. Next, magnetism in FGT will be treated, with special attention to the influence of sample thickness on magnetic ordering and critical behavior. Finally, the basic concepts of ultrafast magnetism are discussed in the context of the (microscopic) three-temperature model, serving as a tool to interpret the results of the time-resolved measurements.

2.1 Magnetic order and phase transitions

As briefly mentioned in the previous chapter, the dimension of a system can have large effects on its magnetic ordering. This section treats how dimension affects the magnetic ordering and critical behavior of a system, using the Ising model as an example. The usefulness of the Ising model related to this work is two-fold; it helps towards an intuitive understanding of the mechanisms behind simple magnetic ordering, while, in particular considering FGT, the model provides a reasonable depiction of reality. Furthermore, the Mermin-Wagner theorem and its consequences for two-dimensional magnetism are discussed. Finally, the effects of various magnetic mechanisms on domain formation and hysteresis in magnetic materials will be discussed.

2.1.1 Ising Model

First, the Ising model [37] will be discussed, which relies on two essential assumptions about the magnetism in a material; (i) the microscopic magnetic moments s_i are fixed on an n-dimensional lattice and (ii) they are only allowed to align along one direction, either spin up ($s_i = \mu$) or spin down ($s_i = -\mu$), with μ the absolute value of a magnetic moment. In particular the former constraint might initially seem an ill approximation of reality. Considering FGT is metallic and the magnetic moments are carried by the conduction electrons, the microscopic magnetic moments can move around relatively freely rather than being strongly pinned down on a rigid lattice. Still, due to the crystallinity of

the FGT lattice, the electrons are localized according to a periodic probability distribution. Especially in the absence of a current, the electrons will remain at relative rest and the maxima of this distribution can be approximated as an Ising lattice. Furthermore, restricting the orientation of magnetic moments along a certain axis is justified by considering the strong magnetic anisotropy of FGT, which heavily favors alignment of magnetic moments along the c-direction (out of plane).

The Hamiltonian $\mathcal{H}$ of an Ising system with N lattice sites can be written as

$$\mathcal{H} = -\frac{1}{2}\sum_{i=1}^{N}\sum_{j=1}^{N} J_{ij} s_i s_j - h\sum_{i=1}^{N} s_i, \tag{2.1}$$

where the first term describes the interaction between magnetic moments using the interaction constant J_{ij} and the second term describes the interaction with a uniform applied magnetic field h. The factor $1/2$ is introduced to correct for double counting of each lattice site.

The Ising model is commonly simplified by taking only nearest-neighbor interactions into account. This approach is justified by considering that J_{ij} describes the exchange interaction, which is caused by the overlap of electronic orbitals and therefore short-ranged. Furthermore, J_{ij} is also independent of lattice site number and will be replaced by the general exchange constant J. With these assumptions, equation 2.1 can be simplified to

$$\mathcal{H} = -\frac{1}{2}J\sum_{i=1}^{N}\sum_{j(i)=1}^{z} s_i s_j - h\sum_{i=1}^{N} s_i, \tag{2.2}$$

where $j(i)$ now represents the nearest neighbors of lattice site i and z is the total amount of nearest neighbors of each lattice site.

Finally, it makes sense to define the magnetization by

$$M = \frac{1}{N}\sum_{i=1}^{N}\langle s_i\rangle = \langle s_i\rangle, \tag{2.3}$$

where it is used that every lattice site has the same expectation value $\langle s_i\rangle$ due to the translational invariance of the system. For ferromagnets such as FGT ($J > 0$), the magnetization also acts as the order parameter of the system, meaning that for $M = 0$, the system is in a disordered state and for $M \neq 0$, the system is in an ordered state.

Equation 2.2 was initially solved in one dimension by Ising for $h = 0$, from which followed that ordering is not allowed at finite temperature [37]. He extrapolated this result to higher dimensions and incorrectly concluded that the Ising model does not allow magnetic ordering in any amount of dimensions. Later, it was shown by Peierls that the 2D Ising model actually does incorporate an intrinsic phase transition [70], after which the presence of magnetic order in 2D was also confirmed by the exact solution from Onsager [71]. This already serves as an indication of the possible vast influence of the dimensionality of a system on (magnetic) ordering.

2.1.2 Weiss Model

The work of Ising was preceded by work from Weiss [72], who proposed the existence of a 'molecular field'[1] to be responsible for the ferromagnetic behavior of a material. His theory is often referred to as 'Weiss field theory' and is equivalent to the result of a mean-field approximation for the Ising Model. In a mean-field approximation, interactions between individual spins are replaced by an average interaction that acts the same on each individual lattice spin.

The accuracy of such a mean-field approximation generally increases for an increasing amount of nearest neighbors of a single lattice spin. Now, considering that the amount of nearest neighbors usually grows with the dimension of a system, mean field theory is expected to be increasingly accurate as the dimension of a system increases. Indeed, many 3D systems are well-described by the Weiss-model [73], which is therefore useful for characterization of the bulk FGT crystal as discussed in section 4.1. To obtain the Weiss model from the Ising model, the mean-field approximation is illustrated in the following.

Considering the Hamiltonian of equation 2.2, the spins s_i can be rewritten as

$$s_i = M + \delta s_i, \tag{2.4}$$

with δs_i the deviation of s_i from its expectation value M. This gives

$$\mathcal{H} = -\frac{1}{2} J \sum_{i=1}^{N} \sum_{j(i)=1}^{z} (M + \delta s_i)(M + \delta s_j) - h \sum_{i=1}^{N} s_i. \tag{2.5}$$

Subsequently, equation 2.5 can be further simplified by assuming small deviations δs_i and using only the linear terms, i.e. $\delta s_i \delta s_j = 0$. Using this approximation and omitting the constant gives

$$\mathcal{H} = -(JMz) \sum_{i=1}^{N} s_i - h \sum_{i=1}^{N} s_i = -h_{\text{eff}} \sum_{i=1}^{N} s_i, \tag{2.6}$$

with $h_{\text{eff}} = JMz + h$ the effective field, being a superposition of the applied field h and the mean field of the spin-spin interactions JMz, where it is recalled that z was defined earlier as the amount of nearest neighbors of a single magnetic moment.

Using the result from equation 2.6 the partition function Z can be constructed as follows,

$$\begin{aligned} Z &= \text{Tr}\left[\exp(-E_i/k_B T)\right] \\ &= \sum_{s_1=\pm\mu} \cdots \sum_{s_N=\pm\mu} \exp\left[-\frac{h + JMz}{k_B T} \sum_{i=1}^{N} s_i\right] \\ &= \left[2\cosh(\mu(h + JMz)/k_B T)\right]^N, \end{aligned} \tag{2.7}$$

where E_i is the energy of microstate i, k_B is Boltzmann's constant and T is the temperature.

[1] Note that the terminology 'molecular field' is of historical origin, it does not correctly describe the physical concepts involved.

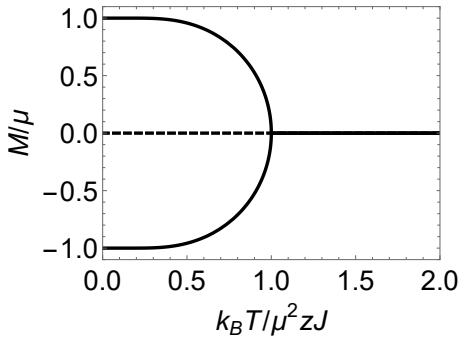

Figure 2.1: The solutions M/μ of the Weiss model from equation 2.8 plotted as a function of T/T_C. All stable solutions are indicated by the solid black lines, the unstable solution $M = 0$ for $T < T_C$ is indicated by the dashed line.

The free energy Ω can be calculated using $\Omega = -k_B T \ln Z$ and can subsequently be related to the (normalized) magnetization via

$$\begin{aligned} m = M/\mu &= -\frac{1}{\mu N}\frac{\partial \Omega}{\partial h_{\text{eff}}} \\ &= \tanh[\mu(h + JMz)/k_B T]. \end{aligned} \tag{2.8}$$

Setting $h = 0$ in equation 2.8 will determine the spontaneous magnetization as a function of T. The solutions for equation 2.8 with $h = 0$ are shown in Figure 2.1. As follows, only one solution exists for $T > \mu^2 zJ/k_B$, giving $m = 0$. For $T < \mu^2 zJ/k_B$ equation 2.8 has three solutions, two non-zero solutions with same absolute value but of opposite sign, and a third solution where $m = 0$. However, the solution $m = 0$ is unstable for $T < \mu^2 Jz/k_B$ [74] and it follows that a net magnetization arises below $T = \mu^2 zJ/k_B$.

This implies that the system goes through a phase transition at this temperature, since the order parameter (M) changes from zero to a non-zero value (or vice versa) when passing this temperature. Hence, it makes sense to define the Curie temperature or critical temperature as

$$T_C = \frac{\mu^2 zJ}{k_B}, \tag{2.9}$$

so equation 2.8 becomes

$$m = \tanh\left[\frac{\mu}{k_B T}h + \frac{T_C}{T}m\right], \tag{2.10}$$

from which the magnetization can be determined in terms of temperature, applied magnetic field and the material-dependent parameters μ and T_C.

2.1.3 Critical behavior and the significance of dimension

A common procedure when considering phase transitions is to express the critical behavior of a system, i.e. its behavior close to the critical point, as a power of $(T - T_C)$. Continuing with the result obtained in the previous section, the

Table 2.1: The values for some of the critical exponents for the 2D Ising, 3D Ising and mean-field universality class. β is the critical exponent of the magnetization and γ is the critical exponent of the magnetic susceptibility. Experimental values were obtained by experiments on 3D fluid systems, belonging to the same universality class as the Ising model. *Adapted from [74].*

Exponent	Mean Field	2D Ising	3D Ising	Experiment 3D Ising
β	1/2	1/8	0.325	$0.316 - 0.327$
γ	1	7/4	1.24	$1.23 - 1.25$

applied field h is set to 0 in equation 2.10, which is then expanded around small m and T close to T_C, yielding

$$m \approx (T - T_C)^{\beta}, \tag{2.11}$$

where β is a so-called critical exponent, equal to 1/2 in the mean-field approximation.

Besides the magnetization, another quantity of interest is the magnetic susceptibility χ which will be used in section 4.1 to determine T_C of the bulk crystal. The power-law behavior of χ can be obtained in a similar way to that of m, using the definition $\chi \equiv \partial M/\partial h$ and approximating the result around small m, h and T close to T_C;

$$\chi \approx |T - T_C|^{-\gamma}, \tag{2.12}$$

where γ is another critical exponent, equal to 1 in the mean-field approximation.

Such critical exponents are often found in proximity to phase transitions and in general, the critical exponent β describes the behavior of the order parameter in any system and γ describes the behavior of its susceptibility to an external perturbation. Besides β and γ, several other critical exponents are used to describe the critical behavior of other quantities such as the heat capacity or correlation length. A remarkable property of such critical exponents is their universality, in the most general case their value only depends on three aspects of a system: [74]

- the symmetry group of the Hamiltonian,
- the dimensionality of the system, and
- the range of the interactions.

Systems sharing these aspects will show the same critical behavior, and are often grouped together in what is called a 'universality class'. As a consequence, systems that initially seem to bear little to no resemblance can behave surprisingly similar in terms of critical behavior. For example, even though the involved physical quantities and interactions are completely different, the critical behavior of the liquid-gas transition is identical to that of the 3D paramagnetic-ferromagnetic phase transition [74].

Considering that dimension is one of the only three aspects that plays a possible role in defining a universality class, it should become clear that it has essential influence on the behavior of a system. Indeed, referring back to the Ising model it is well-known that the critical behavior changes when going from two to three dimensions [74]. In the case of FGT, such a change has also been

observed [44], indicating three- and two-dimensional FGT crystals belong to different universality classes and the ordered phase will therefore behave fundamentally different close to the critical temperature. Furthermore, the mean-field approximation poses its own universality class, showing yet another type of critical behavior. A comparison of β and γ for the 2D, 3D and mean-field Ising model is shown in Table 2.1, of which some values will later be related to the experimental results obtained for FGT.

2.1.4 The Mermin-Wagner Theorem

Another illustrating example of the importance of dimensionality is given by the Mermin-Wagner theorem [35, 36]. This theorem states that ordering is not allowed in any continuously symmetric system of two or less dimensions. At first glance, this might seem a death warrant to two-dimensional magnetism, especially considering the result is exact; it applies to any physical system and its consequences cannot be avoided. However, the result is nuanced and often misunderstood, as will be elaborated on below.

First, the theorem only accounts for *continuously symmetric* systems, i.e. systems where the order parameter can return to its original value via a continuous rotation and/or translation. This means that when discussing magnetic order, it is valid for systems following e.g. a Heisenberg Hamiltonian, where the individual spins are free to point in any direction. On the other hand, mechanisms such as magnetic anisotropy break this continuous symmetry, opening up possibilities for magnetic order to arise. The Ising Hamiltionan discussed in sections 2.1.1 and 2.1.2 is an example of a system incorporating such symmetry breaking and indeed leads to the existence of an ordered phase in two dimensions. Furthermore, magnetic order in two-dimensional FGT is stabilized by its strong uniaxial anisotropy, giving a practical example of such a symmetry broken system.

A second misunderstanding involves the wrong conclusion that absence of order also leads to absence of phase transitions. To understand this, a closer look is taken at the definition of an 'ordered phase'. As discussed earlier, a system is considered to be ordered when the order parameter is non-zero and disordered when it is equal to zero. This does however allow the existence of 'quasi-ordered' phases, where the order parameter is zero, but order is still present in some other form.

An example is encountered in the XY model, a model where the magnetization is free to point in any direction of a 2D plane and is thus continuously symmetric. As described by the Berezinskii–Kosterlitz–Thouless (BKT) transition [75–77], a system following the XY Hamiltonian can undergo a phase transition from a completely disordered state to a quasi-ordered state, where the order parameter remains zero but some level of order appears by the formation of planar vortices, as shown in Figure 2.2.

2.1.5 Domain formation and magnetic hysteresis

At follows from the earlier discussed Ising and Weiss model, magnetic order arises below the Curie temperature in ferromagnetic materials, i.e. materials where $J > 0$. However, in reality macroscopic magnetic order is not always observed in ferromagnets, or the magnetization appears smaller than what would

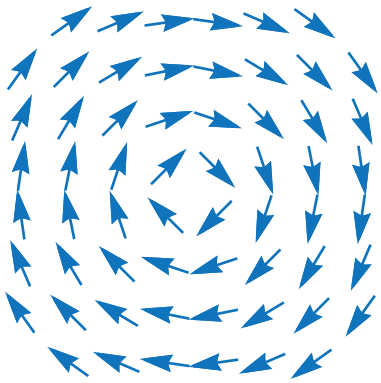

Figure 2.2: An illustrative impression of a planar vortex. The arrows denote the direction of the in-plane magnetic moments.

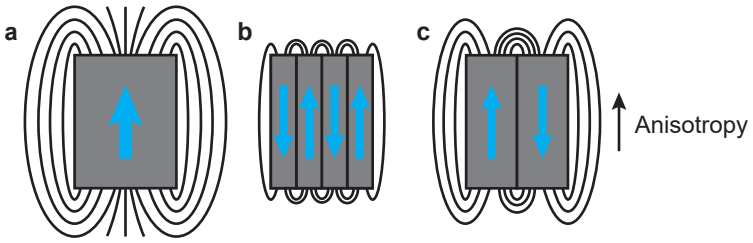

Figure 2.3: An illustration of the stray field for a (a) uniformly magnetized medium, (b) patterned magnetic medium consisting of four domains and (c) patterned magnetic medium consisting of two domains.

be expected from the earlier treated models [73]. This apparent lack or reduction of magnetic order is due to magnetic domain formation of opposing magnetic domains.

Magnetic domain formation follows from the collective magnetic dipole interaction, which is caused by the overlapping stray fields of individual spins. The energy associated with this interaction is referred to as magnetostatic energy and can be reduced by minimizing the stray field, which is the field generated by the magnetic moments outside of a material. Comparing the situation of a uniform magnetic domain as depicted in Figure 2.3a to the configuration shown in Figures 2.3b-c illustrates an intuitive picture of how magnetostatic energy is reduced by the formation of opposing magnetic domains.

On the other hand, the exchange energy in a ferromagnet favors parallel alignment, which is not satisfied at the domain walls, i.e. the borders between opposing magnetic domains. The energy cost associated with such a domain wall is also referred to as the 'domain wall energy', which in ferromagnets generally depends on the exchange energy, possibly in combination with other magnetic mechanisms.

Therefore, a combination of reducing both magnetostatic and domain wall energy leads to the domain formation as illustrated in Figures 2.3b-c, where parallel alignment of the spins is largely maintained, but reduces the stray field around the sample to decrease the magnetostatic energy. The exact size of the

magnetic domains is determined by a competition between the magnetostatic energy and domain wall energy. For example, for relatively small domain wall energy the situation depicted in Figure 2.3b may arise, while for larger domain wall energy the domains develop as sketched in Figure 2.3c, where a relatively larger portion of the stray field is maintained to reduce domain wall energy.

Lastly, many magnetic materials experience some form of magnetic anisotropy, which means that the magnetization has a preference to lie along a specific axis or in a specific plane. As discussed earlier, FGT has a strong, uniaxial, magnetocrystalline anisotropy along the c-direction, which also was implicitly included in the Ising model by demanding the magnetic moments to align either up or down. Consequentially, the anisotropy axis typically determines along which axis opposing magnetic domains prefer to align.

In many materials formation of domains aligned along the anisotropy axis is indeed observed in bulk crystals. However, sufficient reductions in thickness along the anisotropy axis might alter the magnetic behavior, for example leading to the emergence of a single-domain phase [44, 78], as is also observed in FGT. This is due to a reduced amount of magnetic dipoles contributing to the stray field, which reduces the overall amount of energy gain that can be achieved by domain formation. For materials with sufficiently high exchange and anisotropy energy, domain formation can be suppressed in sufficiently thin films, yielding a single-domain phase in thin material layers [73].

Furthermore, anisotropy also influences the magnetostatic behavior of a ferromagnet under the application of an applied field. Due to the Zeeman effect, the magnetization of a magnetic material will generally prefer to align with the direction of an applied magnetic field. However, in the case of an anisotropic material, the magnetization has an intrinsic directional preference along a certain axis or in a certain plane, so the behavior is different for fields applied along an anisotropy axis compared to fields applied perpendicular to an anisotropy axis.

Considering fields applied perpendicular to the anisotropy axis, i.e. the horizontal axis in Figure 2.3, a competition arises between the anisotropy energy and the Zeeman energy due to the applied field. For small fields, this generally results in a canting of the magnetization towards the field direction. Increasing the magnitude of the applied field increases the amount of canting and for high enough fields the magnetization is eventually pulled into the field direction. The magnitude of the applied magnetic field needed to pull the magnetization perpendicular to its anisotropy axis can be used as a measure of anisotropy strength and is usually referred to as the anisotropy field.

In addition, a field can also be applied along the anisotropy axis, i.e. along the vertical axis in Figure 2.3. In the MD phase, the magnetization will again saturate as the field is increased, leading to a SD phase. However, due to the lack of a counter-acting anisotropy mechanism along this axis, saturation will typically occur for much smaller fields compared to the situation where the field is applied perpendicular to the anisotropy axis.

An M, H-curve for the SD phase, where the magnetization uniformly points into one direction, is shown in Figure 2.4, illustrating the emergence of magnetic hysteresis. It is seen that for a certain, large enough field, a sudden switch of the magnetization towards the magnetic field occurs. This sudden switch is into contrast with the slow, coherent switching encountered in the previous situations. This is because the magnetization needs to rotate past the anisot-

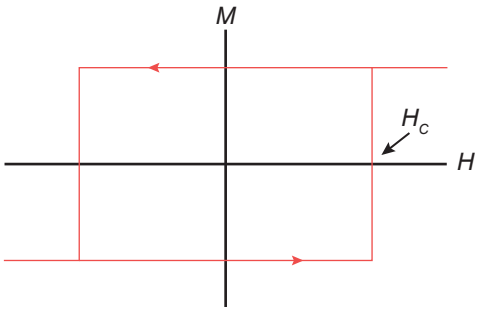

Figure 2.4: An example of a hysteresis loop measured in a single-domain ferromagnet, where the magnetization M is plotted as a function of the applied field H. The arrows denote the direction of the loop and H_c denotes the coercive field.

ropy barrier, creating an initial barrier for the switching that first needs to be overcome by the applied magnetic field. The field for which this switch occurs is referred to as the coercive field, indicated by H_c in the figure.

2.2 Magnetism in Fe_3GeTe_2

In the previous section, general concepts regarding phase transitions and magnetic order were discussed. In this section, these concepts will be applied in more detail to FGT specifically. At first, the influence of crystal thickness (in the c direction) and field-cooling on the magnetic ordering in bulk FGT is discussed, followed by a description of the magnetic behavior of the single-domain phase appearing in thin FGT.

2.2.1 Magnetic ordering in bulk FGT

As follows from literature, magnetic ordering in FGT is largely dominated by three properties, the thickness in the c-direction [44], its strong magnetocrystalline anisotropy [39, 40, 42, 44–46, 79] and the effects of field-cooling [38, 39, 47]. As mentioned earlier in section 1.1, thin films of FGT (< 200nm) exhibit a hard, single domain magnetic phase and as thickness increases, a multi-domain phase emerges. Zooming in on the magnetic structure of the bulk phase, there is, however, more to unravel.

In the first place, previous measurements on magnetization as a function of temperature have shown a difference between field-cooling (FC) and zero-field-cooling (ZFC) behavior of bulk FGT for magnetic fields applied along the c direction [38, 39, 47]. During a ZFC measurement, a ferromagnetic initially at a temperature above T_C is cooled down below T_C, while the magnetization is measured as a function of temperature. A FC measurement is obtained following almost the same procedure, but now a magnetic field, typically in the order of 100mT, is applied along the c-direction when cooling down, while the magnetization is again measured as a function of temperature. For single crystal FGT, both curves are shown in Figure 2.5 and a clear splitting between the curves arises below approximately 180 K.

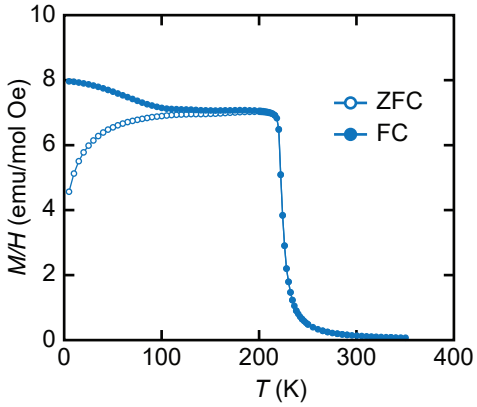

Figure 2.5: The ZFC and FC curves for bulk FGT, measured with the magnetic field along the c direction. *Adapted from [39].*

This type of splitting between ZFC and FC curves typically occurs in strongly anisotropic ferromagnets and follows from domain formation as discussed in section 2.1.5. When bulk FGT is cooled down past T_C during ZFC and for sufficiently slow cooling rates, opposite magnetic domains will form with their magnetization along the anisotropy axis, in accordance with the theory from section 2.1.5. However, in the FC case, the applied field (along the c-axis) introduces an additional energy component favoring alignment not only along this axis, but also specifically in the direction of the applied field. Therefore, the applied field suppresses domain formation and consequentially causes an increase of the magnetization [80]. After removing the field, the anisotropy barrier stabilizes the magnetic moments in their current orientation, causing the obtained alignment to persist.

A magnetic scanning tunneling microscopy (STM) picture of the ZFC and FC domains is shown in Figure 2.6a and 2.6b, respectively. Indeed, below T_C magnetic domain formation is found for ZFC in bulk FGT, as is indicated by the striped lines in Figure 2.6b, providing a top view of the domain formation depicted in Figure 2.3b. Moreover, these domains disappear for field-cooled samples [44, 46, 47], revealing that domain formation is indeed the mechanism behind the splitting between the ZFC and FC curves in Figure 2.5. However, as the crystal thickness increases to micrometer order, surface anomalies appear within the stripe domains for ZFC and a more complicated domain pattern arises for FC [46, 47].

For ZFC, the earlier discussed stripe domains can be distinguished clearly in Figure 2.6a. However, two additional effects occur as well; a repetitive pattern of bubble-like domains appears within the stripe domains and secondly, the domain walls between stripe domains appear wavy. In the case of FC the stripe pattern disappears as illustrated by Figure 2.6b, which can be expected from the earlier discussed effects of field-cooling. However, the magnetic structure still contains other clear features, from which two domain types can be distinguished.

First, the bubble-like domain from the ZFC phase also appears in the FC phase as indicated by the black circle in Figure 2.6b. These domains are scattered over the surface as opposed to the ZFC domains, where they follow a

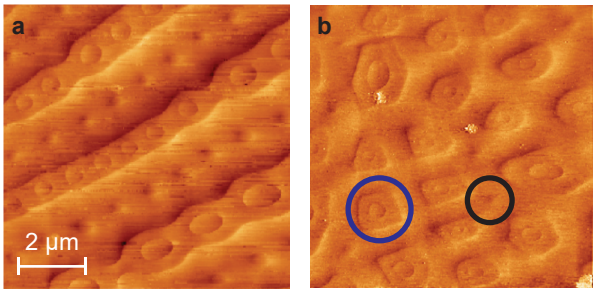

Figure 2.6: STM scans of the ZFC (a) and FC (b) magnetic domains of FGT. Note that the surface of FGT itself is flat and the contrast denotes solely magnetic contrast. The black (blue) circle overlaid on the FC picture indicates the bubble-like (double-walled) domain. The sample has a thickness of $\sim$ 100µm. *Adapted from [47].*

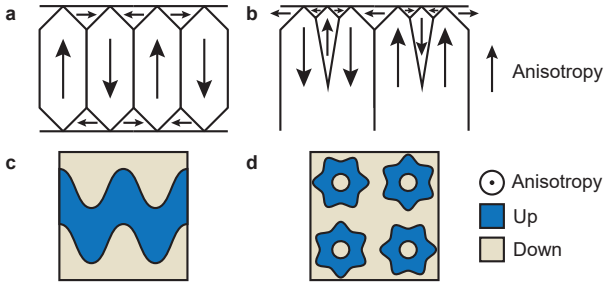

Figure 2.7: Different types of flux closure domain, where (a) and (b) provide a side view and (c) and (d) provide a top view of four different domain types. In (c), the pictured domains penetrate the entire material, although their wavy character is gradually lost towards the bulk, while in (d) the pattern only appears on the surface and evolves towards the bulk in a similar fashion as the spike pattern in (b).

distinct pattern along the stripe domain lines. In addition to these bubble-like domains a second type of domain is formed, which is referred to as a so-called double walled domain and is indicated by the blue circle. Within this domain, the magnetization direction completes 360 degree turn from the outside of a circle towards it center, creating a ring of opposite magnetization.

From the images in Figure 2.6a-b, it becomes clear that field-cooling affects the magnetic structure of FGT, however the magnetic domain patterns do not reflect the simple picture sketched in section 2.1.5. The additional features in the magnetic structure of both the ZFC and FC measurements follow from the formation of so-called flux closure domains, which provide an additional way of reducing magnetostatic energy. Such domains typically occur for increasing thickness, due to the difference in scaling between the involved magnetic energy contributions [80–82]. For example, the domain wall energy scales with the surface between two domains while anisotropic and magnetostatic energy scale with the total volume of a domain. A few examples of different types of flux closure domains are illustrated in Figure 2.7a-d and will be discussed below.

The simplest case of a flux closure domain is shown in Figure 2.7a, which illustrates the formation of perpendicular in-plane domains on the surface of a magnetic material. Such domains help closing the magnetic field loops already inside the material, leading to a reduction field outside the material. However, for highly anisotropic materials such as FGT, a large energy cost is associated with the domains oriented perpendicular to the anisotropy. Highly anisotropic materials can exhibit domain formation as illustrated in Figure 2.7b, where instead of an entire domain switch, a spike-like domain intruding the surface of a material is formed to reduce magnetostatic energy [80]. This is indeed what is seen in FGT, where the bubble-like domains follow this spike character.

The evolution from the simple stripe domains from section 2.1.5 to the more complicated spike-like domains illustrated in Figure 2.7b is exemplary of a general trend; as a material grows thicker, its (surface) domain structure becomes increasingly complicated [82]. Increasing the thickness of a crystal may lead for example to the wavy domain pattern shown in Figure 2.7c, as follows from the model by Goodenough [82]. This pattern is similar to the pattern in Figure 2.3b, except the walls are now curved instead of straight.

Combining the wavy pattern with the spike domains leads to, depending on the competition between the involved magnetic energy terms, either an array of spike domains within the wavy domains or to a surface domain pattern as illustrated in Figure 2.7d [82], where the surface domains fall off towards the bulk in a similar manner as the spike domains. Comparing these patterns to the ZFC and FC domain images for FGT, the former corresponds to the ZFC domains and the latter to the double-walled FC domains, obtained for an applied field along the c-direction. As follows, the domain patterns in both the ZFC and FC case follow from the same origin, but the applied magnetic field distorts the energy balance in such a way that it leads to a different domain shape between both situations.

2.2.2 Magnetic behavior of thin FGT

According to Figure 1.2, a single-domain phase arises in FGT when the thickness is reduced below $\sim 100\,\text{nm}$. This thickness range is of particular interest for this work, since the used measurement setup does not have a sufficiently high resolution to resolve individual domains in the MD phase of thin FGT [44]. In the following, the evolution of the coercive behavior, Curie temperature and critical exponent β will be discussed as a function of flake thickness and temperature, as well as their implications on the magnetic behavior of thin FGT.

The coercive behavior of the SD and MD phase has been characterized in earlier work [44] by measuring hysteresis loops as described in section 2.1.5. The results are shown in Figure 2.8, showing the hysteresis loops for a flake of 3.2 nm (a) and 48 nm (b) thick at various temperatures. For the 3.2 nm flake, the hysteresis loop becomes increasingly small, after which it disappears at the Curie temperature. Therefore, the magnetism in the thin flake goes through a direct transition from the SD phase to the PM phase as temperature increases.

On the other hand, above a certain temperature a linear tail towards the saturation magnetization develops at the end of the hysteresis curve for the 48 nm flake. As temperature increases further, the tail occurs for increasingly smaller fields, eventually appearing already before the field has returned to zero.

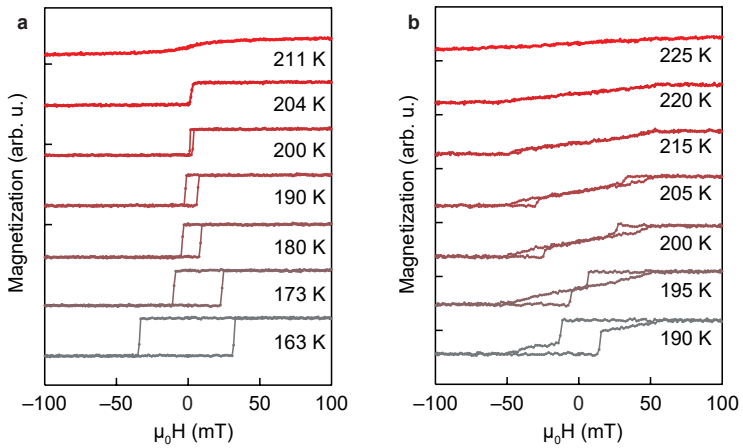

Figure 2.8: The evolution of the hysteric behavior as a function of temperature for FGT flakes of (a) 3.2 nm and (b) 48 nm thickness. *Adapted from [44].*

As follows, no net magnetization prevails at zero field, although some minor loops remain at the edges of the curve. The vanishing magnetization at zero field is associated with the formation of the MD phase [44], as also discussed in section 2.1.5. As the temperature passes T_C, the minor loops disappear as well and the magnetization enters the paramagnetic phase.

In general, two regimes can be distinguished in thin FGT flakes. Flakes with thickness in the order of a few nanometers will undergo a direct transition from the SD to PM phase, while flakes with thickness in the order of tens of nanometers will undergo an intermediate transition to the MD phase before entering the PM phase. Comparing to the phase diagram in Figure 1.2, a rough estimate for the thickness of a flake can therefore be determined by measuring the temperature of either the SD-PM or the SD-MD phase transition.

Furthermore, from five layers down to a single layer, the Curie temperature starts to decrease from around 215 K towards 130 K. This decrease is associated with a crossover from three- to two-dimensional magnetism, which is confirmed by the behavior of the critical exponent β, as shown in Figure 2.9. From Figure 2.9, the bulk value of β appears to be around $\beta = 0.25 - 0.27$ [44]. However, this value is subject to some conflicting reporting, where other authors have determined either a similar value of $\beta = 0.25$ [39] or a larger value of $\beta = 0.327$ [83], which is more in line with the value of the 3D Ising model, $\beta = 0.325$, also listed in Table 2.1.

Nonetheless, Figure 2.9 clearly predicts the formation of a crossover regime for flakes between 2 and 5 layers thick, where T_C steadily declines and $\beta = 0.20 \pm 0.02$ takes an intermediate value between its bulk and monolayer value. Finally, for the monolayer $\beta = 0.14 \pm 0.02$, which corresponds within its error margin to that of the 2D Ising model, $\beta = 0.125$, listed in Table 2.1. This indicates not only a transition from 3D to 2D magnetism, but also a remarkable correspondence between the critical behavior of the Ising model and FGT.

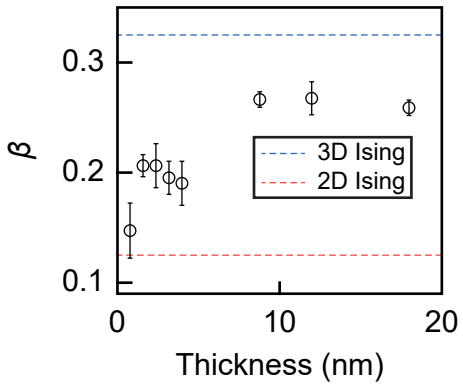

Figure 2.9: The evolution of the critical exponent β as a function of FGT thickness. The critical exponents of the two ($\beta = 1/8$) and three ($\beta = 0.325$) dimensional Ising model are shown by the dashed red and blue lines, respectively. *Adapted from [44].*

2.3 Three-temperature model

A first approach to modeling the ultrafast dynamics of magnetic materials can be achieved by means of the phenomenological three-temperature model (3TM) [50]. This model divides the thermodynamic system of a material in three subsystems as indicated by Figure 2.10, the electron subsystem with temperature T_e, the spin subsystem with temperature T_s and the phonon subsystem with temperature T_p. The magnetization is then determined through the M versus T dependence from for example the Weiss model, where T is replaced by T_s. Subsequently, the interaction between the various systems is described by phenomenological coupling parameters G_{ep}, G_{es} and G_{sp} for the electron-phonon, electron-spin and spin-phonon interactions respectively.

Now, the thermodynamics of a magnetic system can be described by three differential equations [50],

$$\begin{aligned} C_e(T_e)\frac{\mathrm{d}T_e}{\mathrm{d}t} &= -G_{ep}(T_e - T_p) - G_{es}(T_e - T_s) + P(t), \\ C_s(T_s)\frac{\mathrm{d}T_s}{\mathrm{d}t} &= -G_{es}(T_s - T_e) - G_{sp}(T_s - T_p), \\ C_p(T_p)\frac{\mathrm{d}T_p}{\mathrm{d}t} &= -G_{ep}(T_p - T_e) - G_{sp}(T_p - T_s), \end{aligned} \tag{2.13}$$

where C_e, C_s and C_p denote the heat capacities of respectively the electron, spin and phonon system. Since a laser source is used to excite the dynamics, initial heating will be due to hot electrons created by the absorbed laser pulse, so a source term $P(t)$ is included in the electron bath. It should be noted that including the source term in this manner assumes instant electron thermalization [53], while in reality thermalization occurs on a timescale of around 100 fs [51, 53] .

The system described by equation 2.13 can be modeled numerically to study its general behavior. As a boundary condition to equation 2.13, it is assumed that the system is initially in thermal equilibrium, i.e. $T_e = T_s = T_p = T_0$,

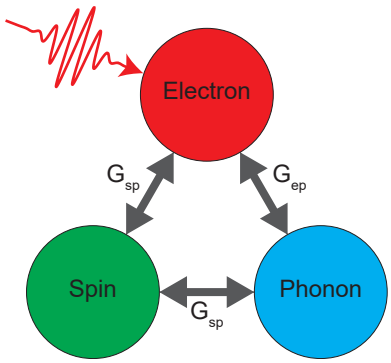

Figure 2.10: A schematic overview of the 3TM model, denoting the temperature baths of the electron, spin and phonon subsystem and the coupling parameters G_{ep}, G_{es} and G_{sp} describing the interactions between the baths. A laser pulse is used to denote the source term $P(t)$.

where T_0 is the ambient temperature. Using the earlier discussed Weiss model, the result for $T_s(t)$ can be substituted as the temperature in equation 2.10 ($h = 0$) to determine the time-dependent magnetization $M(t)$. For the source term $P(t)$ a Gaussian pulse is used.

In Figure 2.11a-b, a typical result of numerically modeling equation 2.13 is shown, where parameters are chosen in such a way that a result similar to the demagnetization of nickel is obtained. Figure 2.11a shows the temporal evolution of the involved temperatures and Figure 2.11b shows the corresponding evolution of the magnetization. As follows, the magnetization experiences a sharp dip, followed by a stabilization at a higher value as the three subsystems mutually relax. As will be discussed later in this section, this type of demagnetization is usually referred to as type I and its characteristics follow from the relative magnitude of two distinct characteristic timescales. These timescales can be derived analytically by solving equation 2.13 under certain conditions, as will be described following a similar approach as in [53, 84].

First, instead of using the source term $P(t)$, heating of the electron system is assumed instantaneous. Therefore, the source term can be omitted from equation 2.13 and its effect can be absorbed into the boundary condition of T_e at $t = 0$. Furthermore, C_e, C_s and C_p are assumed to be independent of temperature, which is valid in the limit of low laser fluence[2] [53]. Furthermore, it is assumed that the heat capacity C_s of the spin system is small and that the dynamics of the electron and phonon system are dominated by their mutual interactions. These assumptions effectively reduce equation 2.13 to a two-temperature system described by

$$\begin{aligned} C_e \frac{\mathrm{d}T_e}{\mathrm{d}t} &= -G_{ep}(T_e(t) - T_p(t)), \\ C_p \frac{\mathrm{d}T_p}{\mathrm{d}t} &= -G_{ep}(T_p(t) - T_e(t)), \end{aligned} \tag{2.14}$$

[2]Laser fluence is the energy of the laser pulse divided by the area of the pumped region.

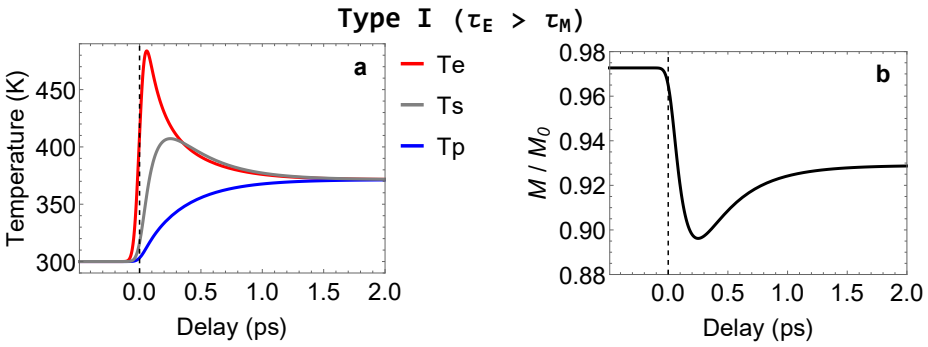

Figure 2.11: A simulated result from equation 2.13 with (a) the evolution of the electron temperature T_e (red), spin temperature T_s (grey) and phonon temperature T_p (blue) as a function of time and (b) the temporal evolution of the magnetization M divided by its saturation magnetization M_0. The magnetization curve in (b) was obtained by substituting $T_s(t)$ from (a) in equation 2.10 (and setting $h = 0$). The demagnetization follows a type I profile, typical for $\tau_E > \tau_M$.

which can be solved analytically, yielding the general solution

$$\begin{aligned} T_e(t) &= A + Be^{-t/\tau_E}, \\ T_p(t) &= A - B\frac{C_e}{C_p}e^{-t/\tau_E}, \end{aligned} \tag{2.15}$$

where $\tau_E = -G_{ep}(1/C_p + 1/C_e)$.

The initial conditions are given by $T_p(0) = T_0$ and $T_e(0) = T_0 + \Delta T_{h,e}$, where T_0 is the temperature of the system before excitation and $\Delta T_{h,e}$ describes the initial heating of the electron system. Furthermore, the quantity $T_e(\infty) = T_p(\infty) \equiv T_0 + \Delta T_1$ is defined to simplify the resulting expression. Lastly, the ratio C_e/C_p can be determined in terms of $\Delta T_{h,e}$ and ΔT_1 by considering that

$$C_e(T_e(0) - T_e(\infty)) + C_p(T_p(0) - T_p(\infty)) = 0, \tag{2.16}$$

yielding

$$\frac{C_e}{C_p} = \frac{\Delta T_1}{\Delta T_{h,e} - \Delta T_1}. \tag{2.17}$$

Equation 2.15 can subsequently be rewritten as

$$\begin{aligned} T_e(t) &= T_0 + \Delta T_1 + (\Delta T_{h,e} - \Delta T_1)\, e^{-t/\tau_E}, \\ T_p(t) &= T_0 + \Delta T_1 \left(1 - e^{-t/\tau_E}\right). \end{aligned} \tag{2.18}$$

Now, having obtained expressions fro $T_e(t)$ and $T_p(T)$, these expressions can be substituted back into equation 2.13, which can then be solved for the spin temperature, giving

$$T_s(t) = T_0 + \Delta T_1 - \frac{(\tau_E \Delta T_2 - \tau_M \Delta T_1)\, e^{-t/\tau_M} + \tau_E\, (\Delta T_1 - \Delta T_2)\, e^{-t/\tau_E}}{\tau_E - \tau_M}, \tag{2.19}$$

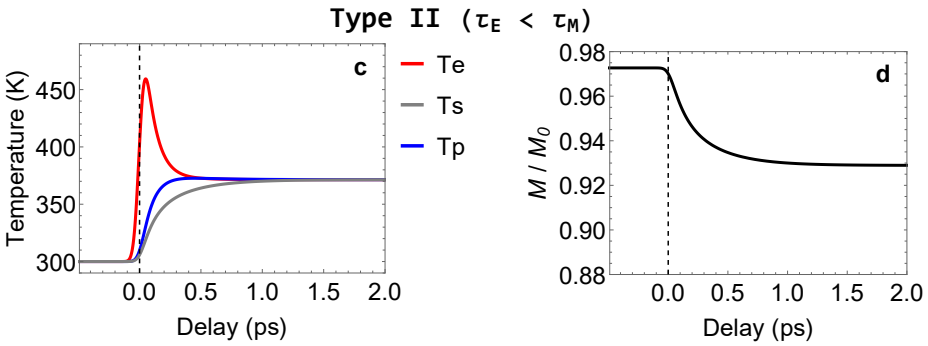

Figure 2.12: A simulated result from equation 2.13 with (a) the evolution of the electron temperature T_e (red), spin temperature T_s (grey) and phonon temperature T_p (blue) as a function of time and (b) the temporal evolution of the magnetization M divided by its saturation magnetization M_0. The magnetization curve in (b) was obtained by substituting $T_s(t)$ from (a) in equation 2.10 (and setting $h = 0$). The demagnetization follows a type II profile, typical for $\tau_E < \tau_M$.

where $1/\tau_M = G_{es}/C_s + G_{sp}/C_s$ and $\Delta T_2 = \Delta T_{h,e}\tau_M G_{es}/C_s$. The appearance of two distinct timescales follows, the electronic timescale τ_E, which describes the relaxation between the electron and phonon system and the magnetic timescale τ_M, which solitarily describes the relaxation from both the electron and phonon subsystem with the spin subsystem.

2.3.1 Type I and type II demagnetization

As shortly referred to earlier, the type of demagnetization process is distinguished by the relative magnitude of the two characteristic timescales, τ_E and τ_M. The characteristic profile of type I demagnetization was shown in Figure 2.11b along with the associated temporal evolution of the three subsystem temperatures in Figure 2.11a. The situation in Figure 2.11a is characteristic for $\tau_E > \tau_M$, originating from rapid thermal relaxation between the electron and spin system via the fast τ_M process, as illustrated in Figure 2.11b, followed by a slower relaxation of the phonon system towards a mutual equilibrium. What follows is an initial dip in magnetization due to the rapid increase in spin temperature followed by a longer relaxation towards a higher equilibrium value.

On the other hand, the situation for $\tau_E < \tau_M$ is shown in Figures 2.12a-b, which is referred to as type II demagnetization. It is observed that the initial dip in the magnetization (Figure 2.12b) has vanished and instead the magnetization steadily declines towards its new equilibrium. As follows, in the type II situation, the electron and phonon subsystem first relax towards a mutual equilibrium via the faster τ_E channel. The relaxation of the spin system with the other two systems then occurs via the longer τ_M process, leading to the steady decline of magnetization as observed in Figure 2.12b.

Comparing the type I to the type II process, the relative magnitude between the two timescales dictates which system is first to reach equilibrium with the heated electron system, illustrating the mechanism behind the two distinct shapes of the type I and type II demagnetization curves.

2.3.2 Microscopic theory behind 3TM

While the exact contributions of the relevant microscopic mechanisms behind the 3TM remain under debate, microscopic models have been proven useful for describing trends and general behavior [85–87]. In this work, the microscopic three temperature model (M3TM) [56] will be employed, which is based on a localized approach using phonon-mediated spin-flip scattering. Although it has been shown that non-local contributions might also affect the demagnetization process [57, 58, 88], a description based on local processes sufficiently explains the observations in this work.

The M3TM builds onto the phenomenological 3TM, maintaining the description of three interacting thermodynamic subsystems, but replacing the phenomenological parameters by quantum-mechanical descriptions of he subsystem energies and scattering processes. The model uses simple approximations for each subsystem; the electron subsystem is described as a free electron gas, the phonon system is described using the Debye model and the spin system is again described by the Weiss model.

The interactions between various subsystems are substituted by two scattering processes; regular electron-phonon scattering between electrons and longitudinal phonons and a scattering mechanism based on an Elliott-Yafett type of scattering. The latter describes how, due to spin orbit interaction, there is a small chance for an electron to flip its spin during an electron-phonon scattering event, therefore providing a channel between the spin system and the electron and phonon systems.

This model can be solved analytically under similar assumptions as the phenomenological 3TM, yielding the following equation of motion for the (normalized) magnetization [56, 61];

$$\frac{\mathrm{d}m}{\mathrm{d}t} = R\frac{T_p}{T_C}m\left[1 - m\coth\left(m\frac{T_C}{Te}\right)\right], \tag{2.20}$$

where T_p and T_e are the respective temperatures of the phonon and electron system, T_C is the Curie temperature and R is a material-dependent constant, which serves as a scaling factor between the electron-phonon and spin dynamics, as discussed in the following.

When R is compared to the electron-phonon relaxation rate at the Curie temperature τ_{E0}, it serves as an indicator of the dominant type of dynamics in a material. Figure 2.13 shows an overview of the relevant dynamics for a range of R values multiplied by $\tau_E 0$. The other axes indicate the temperature T divided by T_C and the q value, which is related to the laser fluence and describes the amount of demagnetization lying between 0 (no demagnetization) and 1 (complete demagnetization).

In general, comparing R to τ_{E0} can be used to qualify the dominant type of dynamics in a material, yielding three different regimes as also illustrated in Figure 2.13. For $R \gg 1/\tau_{E0}$, type I demagnetization is dominant, for $R \sim 1/\tau_{E0}$, a transition from type I and II dynamics occurs for increasing temperature and/or fluence and finally, for $R \ll 1/\tau_{E0}$, type II magnetization is dominant.

A useful approach for determining R experimentally is by measuring the magnetic timescale τ_M as a function of temperature. Using the M3TM model

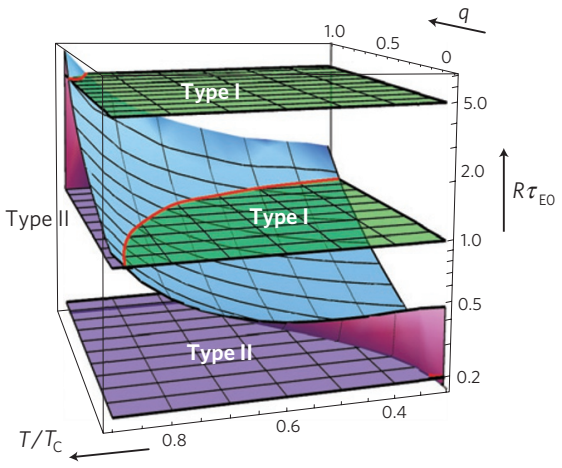

Figure 2.13: The type of magnetization dynamics indicated as a function of temperature T divided by T_C, the product $R\tau_{E0}$ and the q value, which determines the relative amount of demagnetization. The curved plane represents the transition between type I and type II dynamics and the horizontal planes denote the values $R\tau_{E0} = 0.2, 1.0, 5.0$. *Adapted from [56].*

τ_M can be expressed for T close to T_C as follows [61],

$$\tau_M = \frac{1}{2R}\left(1 - \frac{T}{T_C}\right)^{-1}, \tag{2.21}$$

which is valid in the low-fluence limit and will be used in chapter 4 to fit the evolution of τ_M as a function of temperature to determine R for FGT.

Chapter 3

Experimental methods

In this chapter the experimental methods used in this work are elaborated on. In the first section, the sample preparation procedure is outlined, discussing the mechanical exfolation of FGT flakes. Subsequently, the magneto-optical Kerr effect will be treated first on a phenomenological basis after which its microscopic origin will be discussed. In section 3.3, schemes for implementing static and time-resolved MOKE measurements will be discussed including the relevant modulation techniques. Finally, two other experimental techniques used in this work are discussed in the last section, being SQUID magnetometry and energy dispersive X-ray spectroscopy.

3.1 Sample preparation

Thin flakes of FGT were prepared by mechanical exfoliation from the bulk crystal. Since thin layers of FGT are only moderately air-stable [89], exfoliation is performed by use of the scotch-tape method in a glove box under an inert N_2 environment, with O_2 content $< 0.1\,\text{ppm}$ and H_2O content $< 1\,\text{ppm}$. Exfoliation is performed using regular scotch tape, after which the exfoliated flakes are deposited on a degenerately boron doped Si/SiO_2 substrate. The boron doping is mainly used to enhance optical contrast between flakes of different thickness, but also assists in conducting heat away from the flakes after laser pulse excitation. Before exfoliation, magnetic markers of the composition Ta(15)/Pt(15)/Co(1)/Pt(4) were deposited on the substrate using electron beam lithography and sputter deposition. The markers serve multiple purposes, they assist in localizing the FGT flakes and focusing the laser beam (see Appendix A.1), and their magnetic properties are used for initial pump-probe alignment during the time-resolved measurements.

After exfoliation on the substrate, samples were transported in a sealed nitrogen container to a glove bag, where they are examined under a microscope to determine the position and obtain an estimate of the thickness of exfoliated flakes. Taking into account the phase diagram shown in Figure 1.2, flakes should typically be thinner than 100nm to ensure a single-domain FM phase. The flake thickness can be determined by optical contrast, as is also common for other VdW materials [90, 91]. Via this method, the flakes can be roughly characterized in three different classes, as depicted in Figure 3.1a-c. If a flake appears to be

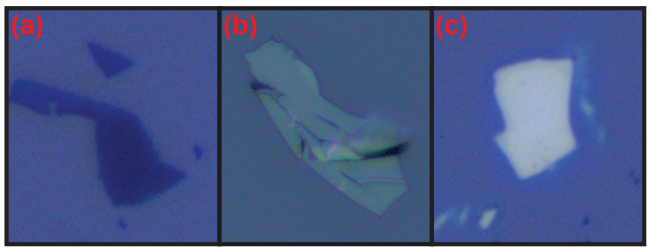

Figure 3.1: An illustration of the three different thickness classes that can be distinguished by optical contrast. (a) A typical flake with thickness in the order of a few nanometers, (b) a typical flake with thickness in the order of several tens of nanometers and (c) a bulk-like flake with thickness greater than 100 nanometer.

clearly darker compared to the substrate (Figure 3.1a), the thickness will be in the order of several nanometers. If the brightness of the flake is comparable or slightly brighter compared to the substrate (Figure 3.1b), it will have a thickness in the order of tens of nanometers. Finally, bulk-like flakes with a thickness $>$ 100nm will appear much brighter when compared to the substrate (Figure 3.1c). The latter are of little purpose to the investigations in this work, concerning the focus is on measurements on the single-domain phase of FGT. Thin flakes are identified under the microscope and their location is noted with respect to the earlier deposited markers.

After having identified suitable flakes and their position, samples are transported back into the glove box, again using the sealed nitrogen container. While still in the glove box, individual samples are mounted in an airtight, continuous flow, sample-in-vacuum cryostat with optical access (for details, see Appendix B.2). A small amount of vacuum grease is used to fixate the sample and ensure proper thermal contact with the cold finger of the cryostat. Afterwards, the cryostat is removed from the glove box, while the sample space remains sealed, and mounted in the optical setup as described in section 3.3. Subsequently, the cryostat, including the sample space, is pumped towards high vacuum ($\sim 10^{-7}$mbar), while ensuring no air flow is present towards the sample space of the cryostat. Following this procedure, the sample will be shielded from air during the entire preparation process to ensure optimal sample quality.

3.2 Magneto-optical Kerr Effect

In this thesis, the so-called magneto-optical Kerr effect (MOKE) will be used as the main experimental method to probe the magnetization of FGT by exploiting the interaction between light and magnetism. A first observation of interaction between light and magnetism was presented by Faraday in 1846 [92], in which it was reported that linearly polarized light passing through a material that is subject to an applied magnetic field, experiences a rotation in polarization. This work was further explored by Verdet, who observed a linear relation between amount of rotation and applied magnetic field [93]. Some years later, Kerr observed a similar effect for light reflecting upon a magnetic material, where light experiences both a rotation in polarization and change in ellipticity upon

reflection [94]. Both the Faraday and Kerr effect find their origin in the same microscopic mechanisms, which will first be described on a phenomenological basis. Afterwards, the microscopic origin will be discussed as well.

3.2.1 Phenomenological description of MOKE

In a phenomenological description, MOKE can be separated into two different parts. First, the polarization of linearly polarized light will experience a rotation upon reflection off a magnetic material, often referred to as Kerr rotation. This rotation follows from the light slightly penetrating a material upon reflection. Its origin is equivalent to that of Faraday rotation and is known as magnetic circular birefringence (MCB). MCB describes how the amount of magnetization in a material causes a difference in refractive index, and thus in propagation velocity, for left- and right-hand circularly polarized (LCP and RCP, respectively) light. Considering that linearly polarized light can be expressed as a superposition of LCP and RCP light, the difference in refractive index will induce a relative phase shift between the two, which translates to a rotation of the linear plane of polarization.

The second part of MOKE comprises a change in ellipticity for light reflecting upon a magnetic material. This change in ellipticity follows from magnetic circular dichroism (MCD), which describes a difference in absorption for LCP and RCP light caused by the magnetization of a material. This means that an initially linearly polarized light ray will gain ellipticity, due to a relative change in amplitude between LCP and RCP components of the light.

Both parts of MOKE can be captured in a single complex rotation angle

$$\Theta = \theta + i\epsilon, \tag{3.1}$$

where θ is the Kerr rotation following from MCB angle and ϵ is the Kerr ellipticity following from MCD. Both the real and imaginary part of this induced angle commonly scale linearly with the magnetization of a material [95]. For simple systems θ and ϵ also scale with the off-diagonal components of the dielectric tensor, yielding a direct relation between the complex MOKE rotation angle Θ and the dielectric tensor of a material.

Lastly, MOKE is not only proportional to the magnitude of the magnetization, but also to its relative orientation to that of the incoming light [95]. Figure 3.2 shows the three possible configurations for MOKE measurements, polar MOKE for out of plane magnetization, longitudinal MOKE for in-plane magnetization along the direction of light travel and transversal MOKE for in-plane magnetization perpendicular to the direction of light travel. In the linearized situation, MOKE only scales with the magnetization component parallel to the direction of light travel, corrected by the (complex) angle of refraction inside the material [95].

It follows that for perpendicular incident light, only the out-of-plane (OOP) magnetization component is measured. Since transversal MOKE is a non-linear effect it is usually much smaller, meaning that for non-perpendicular incidence mainly the polar and longitudinal component of MOKE are obtained. Finally, in the linearized situation for polar MOKE, the relation between the complex angle Θ and magnetization M yields

$$\Theta = \zeta M, \tag{3.2}$$

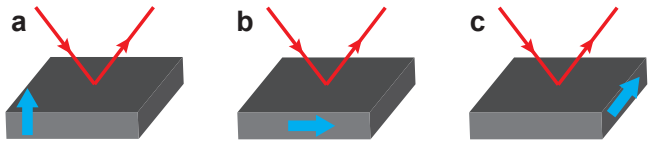

Figure 3.2: Illustration of the three different configurations for MOKE, with (a) polar, (b) longitudinal and (c) transversal MOKE. The red line depicts the incoming and reflected light, the blue arrow depicts the direction of the magnetization vector.

where ζ is a (complex) proportionality constant related to MCB and MCD [95].

Equation 3.2 can be used to directly relate the measured (complex) rotation angle to the magnetization of a material. However, in practice the conversion can be cumbersome, for example due to the non-trivial behavior of the refractive index for very thin layers. Therefore, usually only the relative change in M is calculated and equation 3.2 is used to justify the linear relation between Θ and M.

3.2.2 Microscopic origin of MOKE

In the previous section, MOKE was discussed on a phenomenological basis, but the origin of MCB and MCD was left untreated. As will be explained in this section, the origin of those effects lies in the electronic transitions of a material and their optical selection rules. To provide an illustrative picture, the transitions from an unpolarized p-band to a spin-polarized $3d$-band will be examined. Figure 3.3 provides a simplified picture of the energy levels of a p- and $3d$-band and the allowed optical transitions between the two. To exemplify the mechanisms under discussion, energy level broadening due to band formation is not illustrated.

Starting with the source of the magnetism in the material, the exchange splitting of the $3d$ band between up and down spin is shown by the energy difference ΔE_{ex}, which in the case of d-band splitting is typically is in the order of 1 eV [73]. Subsequently, both sub-bands are further split into five bands due to spin-orbit (SO) coupling. Each of the SO split bands is associated with a separate orbital angular momentum projection, with quantum number m_ℓ in the range $m_\ell = -2, -1, 0, 1, 2$. The magnitude of the SO splitting ΔE_{SO} is typically around 0.05eV when considering the $3d$ band [97].

To determine the relative position of the different bands the SO Hamiltonian

$$H_{SO} = \eta \mathbf{L} \cdot \mathbf{S} \tag{3.3}$$

is used, where η is a positive, material-specific SO coupling constant, $\mathbf{L}$ is the total angular momentum and $\mathbf{S}$ is the total spin. Minimizing H_{SO} constitutes that the lowest energy sub-band in the spin down band corresponds to the largest value for m_ℓ, while for the spin up band the opposite holds and the lowest energy sub-band corresponds to the smallest value for m_ℓ. Lastly, the p-band remains intact and is degenerate in both spin and angular momentum, resulting in a single p-band with $m_\ell = -1, 0, 1$.

Parts of this section were adapted from [96].

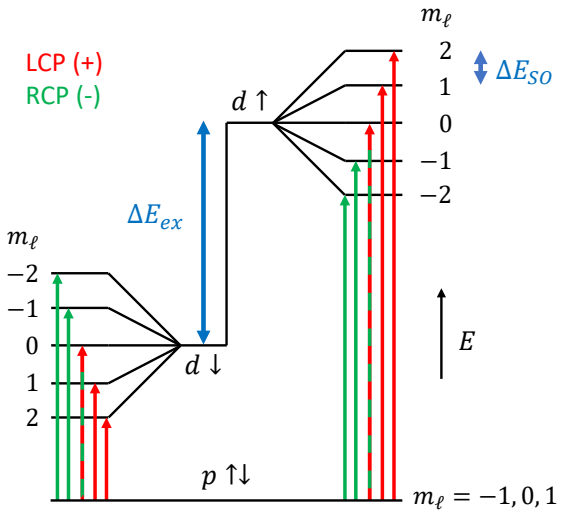

Figure 3.3: A simplified picture of the energy levels of a p- and $3d$-band and the allowed optical transitions between the two. The splitting mechanisms are the exchange splitting ΔE_{ex} and the SO splitting ΔE_{SO}. The spin of a band is depicted by the $\uparrow$ ($\downarrow$) for spin up (down), the choice for the spin down band as majority band is arbitrary and the opposite situation is physically equivalent. The allowed optical transitions are depicted by the arrows in red (green) for LCP (RCP) light. Note that the transitions towards the two $m_\ell = 0$ levels is allowed for both LCP and RCP, hence their mixed color pattern of both red and green. Band broadening of the energy levels was omitted for clarity.

Due to conservation of angular momentum, the transitions between the p and $3d$ band are optically polarized, i.e. certain bands are accessible by only LCP or RCP light. This can be explained by looking at the angular momentum projection of the p electrons along the spin angular momentum of a photon, $\sigma_{\pm} = \pm 1$, where the $+$ $(-)$ stands for LCP (RCP) light. It is assumed that the spin-flip probability is negligible, i.e. $\Delta s = 0$, meaning that only the orbital angular momentum projection m_ℓ of the electron changes upon absorption of the photon. The photon will either add or subtract one quantum of angular momentum depending on its polarization, yielding

$$m_{\ell,p} - m_{\ell,3d} = \pm 1, \tag{3.4}$$

where the subscripts p and $3d$ denote m_ℓ of the p ground state and $3d$ excited state following a transition.

It follows from the selection rule given by equation 3.4 that for a photon with angular momentum $\sigma_{\pm} = \pm 1$, the excited states with $m_{\ell,3d} = \mp 1, 2$ are not accessible, leaving only three allowed transitions for each polarization as illustrated by the red (LCP) and green (RCP) arrows in Figure 3.3. As a consequence, a difference in absorption between LCP and RCP light arises depending on the wavelength of the light and the SO and exchange splitting. The latter is also responsible for the magnetism in a material and via this way the difference in absorption for LCP and RCP light provides a direct probe to the magnetization of the material, leading to the earlier discussed magnetic circular dichroism.

The origin of magnetic circular birefringence can also be found in the optical transitions of a material, however its connection is not as intuitive as for MCD. This follows from birefringence being related to the electronic structure in a less straightforward way compared to dichroism. On the contrary to dichroic effects, birefringent effects occur for light that has a wavelength not in resonance with the relevant electronic transitions. In general, the refractive index is proportional to the resonance between the photon energy of the incoming light and the energy gap between optical transitions [98, 99]. For the earlier discussed polarized transitions, this results in a different resonance conditions for LCP and RCP light. Consequentially, the refractive indices for LCP and RCP light will not be equal leading to the earlier discussed MCB. An in-depth description of (magnetic) circular birefringence is outside of the scope of this work, but more details on the relation between the electronic structure and birefringence can be found in [98] and a classical description description of MCB can be found in chapter 20 of [100].

3.3 Setup for (TR-)MOKE measurements

This section discusses a practical implementation of MOKE to measure the (time-resolved) magnetization of a material. A general experimental approach for measuring static MOKE will be discussed first and will subsequently be extended to include time-resolved measurements.

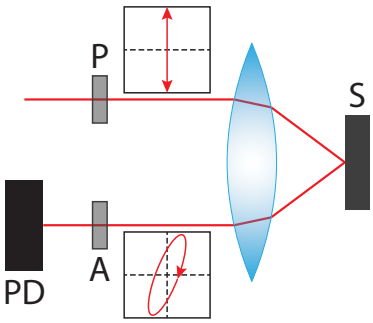

Figure 3.4: A schematic overview of the static MOKE setup. Light passes through a polarizer P, reflects on a sample S, passes the analyzer A and is captured by a photodetector PD. The top graph indicates initial light polarization and the other graph indicates the light polarization after reflection off the sample.

3.3.1 Simple MOKE scheme

A schematic illustration of the most basic MOKE setup is shown in Figure 3.4, employing a crossed-polarizer configuration to measure the polarization induced by the sample. The evolution of the electric field vector will be traced using the Jones matrix formalism [101], largely following the approach described in [61] and [102]. Unpolarized light passes first through a polarizer P, resulting in a linear polarization, which in terms of Jones vectors is given by

$$\mathbf{E_0} = \begin{pmatrix} E_0 \\ 0 \end{pmatrix}, \tag{3.5}$$

where $\mathbf{E_0}$ is the electric field after initial polarization and E_0 is its absolute value.

Subsequently, the light reflects off the sample gaining a complex rotation Θ following from equation 3.1. A rotation of a linearly polarized wave over an angle α can be expressed in the Jones formalism as a rotation matrix

$$R(\alpha) = \begin{pmatrix} \cos\alpha & -\sin\alpha \\ \sin\alpha & \cos\alpha \end{pmatrix}. \tag{3.6}$$

Since Θ is usually small, in the order of millidegrees [95], equation 3.6 can be simplified using the small angle approach ($\sin\alpha = \alpha$, $\cos\alpha = 1$). Furthermore, the reflectivity r of the sample is also accounted for by multiplying the reflectivity matrix by $\sqrt{r}$. The resulting reflection matrix S of the sample then yields

$$S = \sqrt{r}R(\Theta) \approx \sqrt{r}\begin{pmatrix} 1 & -(\theta + i\epsilon) \\ \theta + i\epsilon & 1 \end{pmatrix}. \tag{3.7}$$

Lastly, the light travels through the analyzer A, which is another polarizer under a different angle compared to P. The Jones matrix of a polarizer under an angle α is given by

$$P(\alpha) = \begin{pmatrix} \cos^2\alpha & \cos\alpha\sin\alpha \\ \cos\alpha\sin\alpha & \sin^2\alpha, \end{pmatrix} \tag{3.8}$$

which can be used as an expression for the analyzer.

After the light passed the last analyzer, its Jones vector $\mathbf{E_{det}}$ at the photodetector PD is given by

$$\mathbf{E_{det}} = P(\alpha)S\mathbf{E_0}, \tag{3.9}$$

from which the intensity at the photodetector I_{det} can be calculated

$$\begin{aligned} I_{det} &= |\mathbf{E_{det}}|^2 \\ &= E_0^2 R\left[\cos^2\alpha + (\epsilon^2+\theta^2)\sin^2\alpha + \theta\sin 2\alpha\right] \\ &\approx I_0 R\left[\cos^2\alpha + \theta\sin 2\alpha\right], \end{aligned} \tag{3.10}$$

where $I_0 = E_0^2$ is the initial intensity, $|\ldots|$ denote the absolute value and θ and ϵ are again assumed to be small. It follows that the relative contribution of θ to the signal at the detector is maximized for $\alpha = \pi/2$, however, this would remove θ entirely from equation 3.10 due to the multiplication by $\sin 2\alpha$. Therefore, equation 3.10 is expanded around $\alpha = \pi/2$, yielding

$$I \propto 2\theta\Delta\alpha + \Delta\alpha^2, \tag{3.11}$$

where $\Delta\alpha$ denotes the small deviation from $\alpha = \pi/2$ and I is now proportional to the Kerr rotation angle θ.

3.3.2 Polarization modulation

In principle, the approach described above can be used to measure Kerr rotation. However, the rotation angle is usually small, so a modulation technique is used to improve the signal-to-noise ratio (SNR). A straightforward way to do so is by using a photoelastic modulator (PEM), which modulates the polarization of the light. The result is an oscillation of the polarization between linearly and elliptically polarized light at a certain modulation frequency ω, which is set to 50kHz for all MOKE measurements in this thesis. Locking in on the modulation frequency ω using a lock-in amplifier (LIA) then reduces polarization independent effects, which for example include the regular reflectivity of the sample and electronic noise from the detector.

The PEM is placed after the light has passed through the polarizer, as indicated in Figure 3.5. The Jones matrix of a PEM with its fast axis along the x-axis and its modulated axis along the y-axis is given by

$$R_{\mathrm{PEM}}(t) = \begin{pmatrix} 1 & 0 \\ 0 & e^{iA\cos\omega t}, \end{pmatrix} \tag{3.12}$$

where t is time and A is the retardance, denoting the modulation amplitude in terms of phase difference between RCP and LCP light components. To ensure the light is modulated between LCP and RCP light for $A = \pi/2$, the PEM should be placed under an angle of 45° with respect to the polarization of the incoming light [51]. The Jones Matrix $M(t,\alpha)$ describing the PEM under an angle α can be obtained by $M(t,\alpha) = R(\alpha)R_{\mathrm{PEM}}(t)R(-\alpha)$.

Furthermore, the PEM also induces a time-dependent birefringence on the light, which should be filtered by placing the analyzer correctly. For $\Theta = 0$, the intensity on the detector should therefore be constant, yielding

$$\left(\frac{\mathrm{d}I_{det}}{\mathrm{d}t}\right)_{\Theta=0} = 0, \tag{3.13}$$

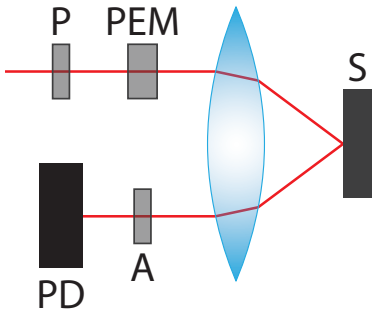

Figure 3.5: A schematic overview of a static MOKE setup similar to that in Figure 3.4, but now includes a photoelastic modulator (PEM).

giving

$$\alpha_{PEM} = \alpha_A + \frac{\pi n}{2}, \tag{3.14}$$

where α_{PEM} and α_A are the angles of the PEM and analyzer respectively and n is an integer. Equation 3.14 states that the analyzer should be aligned parallel to one of the two PEM axes. Since all configurations from equation 3.14 are equivalent, the analyzer and PEM are chosen to be aligned parallel.

The intensity on the detector can now be determined analogous to equation 3.10, again using that θ and ϵ are small, giving

$$I_{det} = \frac{I_0 R}{2}\left(1 + 2\theta\cos\left[A\cos(\omega t)\right] - 2\epsilon\sin\left[A\cos(\omega t)\right]\right). \tag{3.15}$$

Which can be expanded into spherical harmonics using the Jacobi-Anger expansion [103], giving

$$\begin{aligned} I_{dc} &= I_0 R\left[\frac{1}{2} + \theta J_0(A)\right], \\ I_{1f} &= -2\epsilon I_0 R J_1(A)\cos(\omega t), \\ I_{2f} &= -2\theta I_0 R J_2(A)\cos(2\omega t), \end{aligned} \tag{3.16}$$

where I_{dc}, I_{1f} and $I_2 f$ are the the zeroth, first and second harmonic respectively and J_n is the nth Bessel function of the first kind. It follows that ϵ and θ can readily be extracted by entering the output of the photodetector in the lock-in amplifier and locking in on the first (ϵ) or second (θ) harmonic of the PEM frequency ω.

3.3.3 Time-Resolved MOKE measurements

The MOKE scheme as described in the previous section provides a good method of measuring static magnetic behavior. However, it does not offer time resolution to study the ultrafast magnetization dynamics of FGT, which is expected to occur on (sub-)picosecond timescales. Pump-probe spectroscopy can be used to access the dynamics on these ultrafast timescales by employing femtosecond laser pulses [53]. The idea behind pump-probe spectroscopy is illustrated in Figure 3.6, where as an example the simulated curve from Figure 2.11 is used.

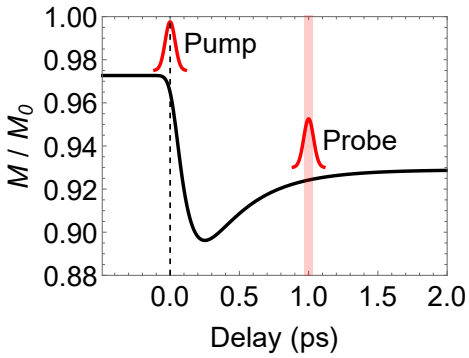

Figure 3.6: An illustration of how pump-probe spectroscopy can be used to measure the magnetization using ultrafast laser pulses. The pump pulse excites the dynamics at $t = 0$ and the probe pulse measures a small part of the excited dynamics at a later time. The curve can experimentally be constructed by varying the delay between pump and probe pulse.

A pump pulse arriving at $t = 0$ excites the the dynamics as described in section 2.3. Shortly after arrival of the pump pulse, a probe pulse arrives at time $t = \Delta t$, probing the state of the system at that instance. Since each pump pulse will excite the same dynamics, repeating the measurement for different values of Δt allows reconstruction of the curve in Figure 3.6.

A schematic illustration to implement such a scheme is shown in Figure 3.7. A mode-locked oscillator is used to generate a pulsed laser beam, with pulse lengths of around $60 - 70$fs and a repetition rate of 82MHz (for details, see Appendix B.1). A beam splitter (BS) is then used to split each pulse into a high-intensity pump and low-intensity probe pulse and a relative delay between the two is induced by inserting a mechanically controlled delay line in the pump path. By adjusting the length of the delay line (DL), the relative difference between the arrival time of the pump and probe pulse can be controlled with a resolution of $\sim 3\,\mu\mathrm{m\,fs}^{-1}$. Both beams are then focused through a single objective onto the sample, which is inside the previously discussed cryostat. The focus was determined by measuring the spot size of the laser beam in accordance with Appendix A.1. Afterwards, the reflected pump beam is blocked and the probe beam is guided to a photodiode.

To measure the magnetization, the same scheme as discussed in section 3.3.2 is introduced in the probe path. However, since the demagnetization signal is usually small compared to the magnetization itself, it has proven useful to filter pump-induced effects using a dual modulation scheme. To do so, a mechanical chopper is placed in the pump path and the pump beam is modulated at a frequency sufficiently far away from the PEM frequency, in this thesis a typical frequency of ~ 70Hz is used. The output from the first LIA is then sent through a second LIA that is referenced at the chopper frequency. Since it is the pump beam that is modulated by the chopper frequency, only the pump-induced effects present in the probe signal will be extracted by the second LIA.

The extracted pump-induced signal contains, besides MOKE, other pump-induced effects such as transient reflectivity [51]. Fortunately, such effects can be filtered out by considering that the magnetic part of the signal switches sign

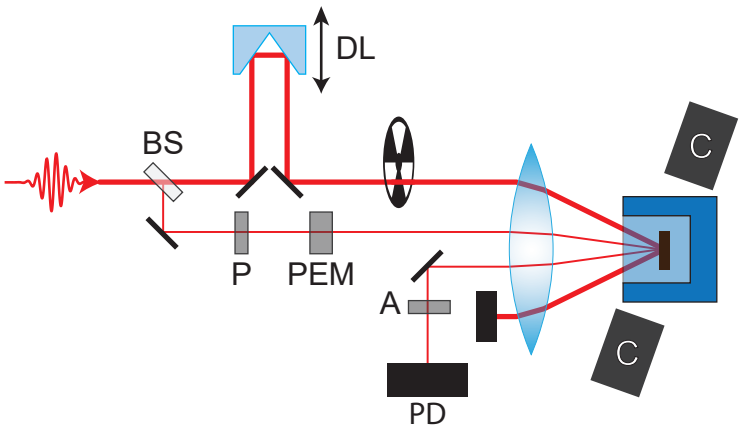

Figure 3.7: A schematic illustration of the used pump-probe scheme. A pulsed laser beam is split by the beam splitter BS into a high-intensity pump and low-intensity probe beam. The pump beam passes the delay line DL and chopper, after which it enters the objective and is focused on the sample, its reflection is subsequently blocked by a beam blocker. The probe beam goes through a similar scheme as depicted in Figure 3.5, passing a polarizer P and photoelastic modulator (PEM) before being focused on the sample, after which the reflection passes the analyzer A and is captured by the photodector PD. Electromagnetic coils (C) are placed around the sample to apply magnetic fields.

for opposite magnetization directions, while the non-magnetic part does not. Subtracting the signals obtained for opposite magnetization directions therefore returns only the magnetic part, whereas addition returns the non-magnetic part. To be able to switch the magnetization, two electromagnetic coils (labeled C in Figure 3.6) are placed around the sample. These coils are furthermore used to perform static characterization by measuring hysteresis loops. The maximum out-of-plane magnetic field angle that can be obtained in this configuration is around 20°, since for larger angles the coils will block the laser beam. However, due to the high anisotropy of FGT it is expected that the OOP component of the field will play a dominant role in aligning the magnetization.

The resulting curve yields the time-dependent magnetization signal after excitation by a laser pulse. As a final step, the time-dependent curve can be normalized to determine the amount of demagnetization with respect to the initial magnetization. To do so, hysteresis loops are measured while the sample is actively being pumped by the pump beam. First, a hysteresis loop is measured with the probe at negative time delay, e.g. by placing the probe at $t = -0.5\,\text{ps}$ in Figure 3.6. A second loop is then measured around maximum demagnetization, e.g. $t = 0.25\,\text{ps}$ in Figure 3.6. An example of such a measurement is illustrated in Figure 3.8, where it is seen that the quenching of the magnetization shows up as a reduction in the step size of the hysteresis loop. The ratio between both step sizes gives the relative amount of demagnetization at $t = 0.25\,\text{ps}$, which can be used to normalize the entire curve with respect to the magnetization before arrival of the pump pulse [1].

[1] A correction should be made to account for the Gaussian shape of the pump and probe beam, which is discussed in Appendix A.2

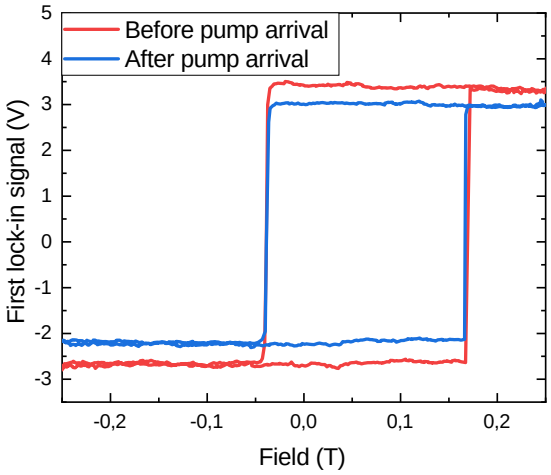

Figure 3.8: An example of two different hysteresis loops measured with the probe beam at various time delays. The red curve is measured before arrival of the pump pulse, e.g. at $t = -0.5\,\mathrm{ps}$ in Figure 3.6 and the blue curve is measured after arrival of the pump pulse at maximum demagnetization, e.g. at $t = 0.25\,\mathrm{ps}$ in Figure 3.6.

3.4 Other experimental techniques

Besides (TR-)MOKE, two other techniques were used for the measurements in this work, being SQUID magnetometry and energy dispersive x-ray spectroscopy. Both techniques will be elaborated on in this section.

3.4.1 SQUID

The bulk FGT crystal is characterized using a superconducting quantum interference device (SQUID). A SQUID is a magnetometer operating on a modified principle of magnetic induction, using superconducting rings containing Josephson junctions [104–106]. In this way, sensitivities greater than $10^{-12}\mathrm{A\,m^2}$ can be achieved [73]. The SQUID will be used to characterize the magnetization of bulk FGT as a function of temperature and applied field, which will be useful for determining its bulk Curie temperature. The operating principle of the SQUID is elaborated on in the following.

First consider a Josephson junction, which consists of two superconducting materials and an insulating barrier between them (see Figure 3.9a), which is thin enough to allow tunneling of electrons across the barrier. In the superconducting state (considering $T = 0$), the electrons on each side of the junction are described by a single wave function ψ_i with $i = 1, 2$ for the left and right side of the junction, respectively. It follows [107, Ch. 21] that the current J across the barrier under an applied voltage V is described by the Josephson equations

$$\begin{aligned} J &= J_0 \sin\delta, \\ \delta(t) &= \delta_0 \frac{2e}{\hbar} \int V(t)dt, \end{aligned} \tag{3.17}$$

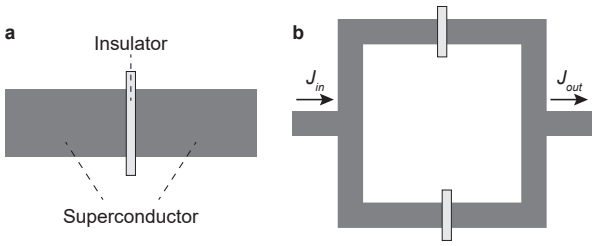

Figure 3.9: (a) A Josephson junction consisting of two superconductors with a thin insulating barrier in-between. (b) A superconducting ring split up by two Josephson junctions, which is the basic working principle of a SQUID.

where J_0 is a junction-dependent constant, δ is the phase difference between ψ_1 and ψ_2, δ_0 is δ at $t = 0$, e is the elementary charge and $\hbar$ is the reduced Planck's constant $h/2\pi$. This leads to a peculiar consequence; in the case of a constant applied voltage V_0, the current across the barrier will oscillate very rapidly. For example, applying 1V across the barrier yields a frequency of $10^{15}\mathrm{s}^{-1}$, which effectively means no measurable current is present. However, without any field applied a non-zero current emerges depending on the initial phase difference between the electrons on each side which. Rather counter-intuitively, this current *disappears* when a voltage is applied.

Subsequently, two Josephson junctions are integrated into a superconducting ring, as depicted in Figure 3.9b. Applying a magnetic field perpendicular to the ring will result in a quantization of the magnetic flux through the ring in terms of the magnetic flux quantum $\Phi_0 = \pi\hbar/e$ [108–110]. Any deviations from (a multiple of) this quantum will be screened by a screening current appearing inside the loop. The magnitude of this screening current is equal for both the top and bottom path, however it is of opposite sign between the two paths. This means that it adds to the Josephson current through one junction and subtracts from the Josephson current through the other junction. Concerning that the charge density is approximately constant, this yields a difference in phase difference between the electron wave functions of the two paths [107, Ch. 21]. Recalling equation 3.17, the current for each different path will therefore be modified and the output current will be constructed by simply adding both currents for the individual paths. However, due to their phase difference induced by the magnetic field, they no longer interfere completely constructively, leading to a reduction in magnitude of the output current.

The difference of magnitude between input and output current is therefore directly associated with the magnitude of the screening current, going from its minimum value to its maximum value in the range of only half a magnetic flux quantum. This means that measuring the voltage associated with the difference between the input and output current [106] provides a sensitivity to magnetic field variations well below Φ_0/A, with A the area of the ring.

The description above provides a basic scheme to measure the magnetization using a SQUID. The SQUID used for this work has its functionality improved by using multiple coils, vibrating-sample techniques [111] and the possibility to apply a magnetic field up to 7T during measurements.

3.4.2 Energy-dispersive X-ray spectroscopy

Energy dispersive X-ray spectroscopy (EDX, EDS or EDXS) is a technique used to measure the elemental composition of a material by measuring element-specific transitions between inner-shell electrons. In this work, it will be used to characterize the local chemical composition of bulk FGT crystals. EDX is usually performed inside an electron microscope, for which in this work a scanning electron microscope (SEM) was used.

The SEM is used to irradiate a sample with a high-energy beam of electrons, ejecting inner-shell electrons from an atom and leaving a vacancy in the specific shell. This vacancy is subsequently filled by another electron from a higher energy shell, accompanied by the emission of an X-ray. By measuring the X-ray spectrum during bombardment, certain element-specific peaks will appear in the spectrum depending on the elemental composition of the material. These peaks can subsequently be fitted from which the relative abundance between elements can be obtained.

EDX has several advantages over other techniques. It can be installed with relative ease in most SEM systems by attaching an X-ray spectrometer and a measurement is fast and straightforward, taking only several minutes. Furthermore, since a SEM is used to excite the electrons, the technique can be applied at a relatively local scale allowing for spatially resolved elemental analysis, although scattering within the sample usually limits the resolution to a few micrometers [112]. Lastly, EDX is also relatively precise, with accuracies up to 0.1% [112].

Chapter 4

Results and discussion

Having discussed the relevant theory in chapter 2 and the employed experimental methods in chapter 3, the obtained experimental results can be readily discussed. Measurements were performed on FGT crystals and flakes from two growth batches, batch I and batch II respectively. In the first section, the bulk characterization of batch II will be described by using results obtained with SQUID and EDX measurements, yielding the Curie temperature and elemental composition of the crystals. Subsequently, thin flakes of FGT are characterized using static MOKE, which is used to verify the perpendicular magnetic anisotropy, discuss domain formation in FGT and study the effects of field cooling. Finally, the results obtained using TR-MOKE are discussed, yielding the first observation of ultrafast demagnetization in a VdW ferromagnet. The evolution of the characteristic timescales involved in the demagnetization process are then investigated as a function of temperature, concluding the experimental content of this work.

4.1 Characterization of the bulk crystal

Before the start of this work, the Curie temperature of the crystals from batch I was characterized using SQUID, yielding $T_C = 217 \pm 5\,\mathrm{K}$, corresponding well to the literature value of 220 K - 230 K. In the following, a similar procedure and its results are described to characterize the Curie temperature of the batch II crystals.

To measure T_C, the crystal is mounted into the earlier discussed SQUID magnetometer, which can measure the magnetization M of the crystal as a function of temperature T. To determine the Curie temperature, the magnetization of the crystal was measured within the temperature interval between 10 and 300 Kelvin. To suppress domain formation and ensure a uniformly magnetized sample, a field of 500 mT was applied along the c-direction during the measurement, i.e. a field-cooling measurement was performed. The result is shown in Figure 4.1 and the Curie temperature can be determined by fitting the earlier obtained Weiss magnetization curve from equation 2.10, yielding $\mu = 6.5 \pm 0.2\mu_B$ and $T_C = 197.7 \pm 0.2\,\mathrm{K}$, where the errors denote the standard error derived from the fit.

However, a clear deviation between fit and experimental data develops as the

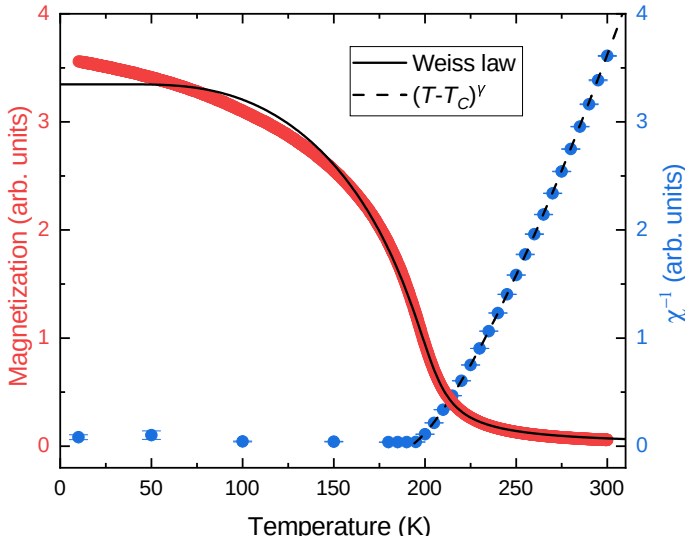

Figure 4.1: The magnetization (red) and inverse magnetic susceptibility (blue) of bulk FGT measured as a function of temperature. Data was collected using a SQUID. During the magnetization measurement, a field of 500mT was applied to align the domains in the FMII phase and the Weiss model was fitted through the magnetization data. The susceptibility for each data point was obtained by doing a small field sweep in a SQUID and calculating χ from the M,H-diagram for each data point. Equation 4.1 was fitted through the susceptibility data.

temperatures further decreases below T_C. Furthermore, according to literature μ should be anywhere in-between $1\mu_B$ and $4.5\mu_B$ [41], which is well below the fitted value. Repeating the fit for $\mu = 1\mu_B$ and $\mu = 4.5\mu_B$ yields $T_C = 205.2 \pm 0.2\,\mathrm{K}$ and $T_C = 200.3 \pm 0.1\,\mathrm{K}$, respectively. As follows, the Weiss model yields a good first estimate of T_C but does not yield a reliable value for T_C despite its seemingly small standard error when fitting. Both T_C and its small error value as obtained from the fitted curve are therefore misleading, since the fitted model itself does not sufficiently describe reality.

To obtain a more reliable value of T_C, an additional approach was used by measuring the magnetic susceptibility χ as a function of temperature. For this, the magnetization was measured during a small field sweep between -10 to $+10\,\mathrm{mT}$ of the applied field H. The susceptibility can then be determined by fitting the relation $M = \chi H$. Repeating this procedure at various temperatures yields the result as shown in Figure 4.1, where the inverse susceptibility is plotted as a function of temperature. In the FM phase, χ is large, so χ^{-1} can be taken approximately zero, while in the PM phase χ can be described using the in section 2.1.3 discussed power law behavior from equation 2.12, yielding

$$\chi^{-1} \propto \begin{cases} (T - T_C)^\gamma, & T \geq T_C \\ 0, & T < T_C \end{cases}, \tag{4.1}$$

where γ is the critical exponent of the susceptibility.

Equation 4.1 can be fitted through the susceptibility data in Figure 4.1, yielding $T_C = 191 \pm 2\,\mathrm{K}$ and $\gamma = 1.3 \pm 0.1$. The value of γ corresponds well

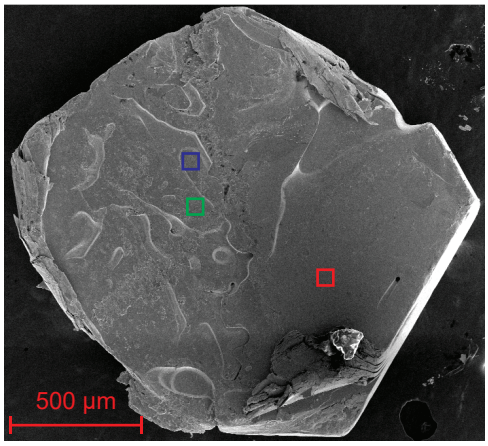

Figure 4.2: A SEM image of the bulk FGT crystal used for EDX measurements. Measurements were performed at three areas inside the colored rectangles.

with the literature value for the 3D Ising model as listed in Table 2.1, however the Curie temperature is found to be around 20 % below its literature value. A similar reduction of T_C has also been observed in earlier work and is often associated with an iron deficiency of the Fe-II site [38, 41, 45], which forms the hexagonal lattice with Ge atoms.

To verify such a possible iron deficiency, EDX was performed on a piece of bulk crystal shown in Figure 4.2. Measurements were conducted on three different areas of 50 µm × 50 µm, as indicated by the colored rectangles. The resulting composition was normalized on the abundance of tellurium[1], yielding $Fe_{2.73(4)}Ge_{1.17(2)}Te_2$, $Fe_{2.99(4)}Ge_{1.04(1)}Te_2$ and $Fe_{2.94(4)}Ge_{1.11(2)}Te_2$ for the red, green and blue rectangle respectively. As follows, the crystal is indeed iron deficient, explaining the deviation of T_C from its literature value. In addition, the deficiency is found the be non-uniform across the crystal, which has possible effects on the magnetostatic behavior of thin FGT as will be discussed in section 4.2.

4.2 Magnetostatic measurements on thin FGT

Subsequently, thin flakes were exfoliated from the bulk crystal and deposited on the substrate in accordance with the procedure listed in section 3.1. Initial measurements were performed on a flake exfoliated from batch I crystals, for which a microscope image is shown in Figure 4.3a. The red encircled region was identified to be sufficiently thin using optical contrast as described in section 3.1, and is therefore used for measurements.

First, the magnetic remanence of the flake was measured, which is the amount of magnetization that persists after the application and subsequent removal of a magnetic field. The result is shown in Figure 4.3b-c after application of a positive (b) and negative (c) field. The measurement was obtained by

[1]This approach is validated by considering that the abundance of Te was mostly constant over the different measurements, with an average of 2.00 ± 0.03, where the standard deviation is attributed to the measurement error.

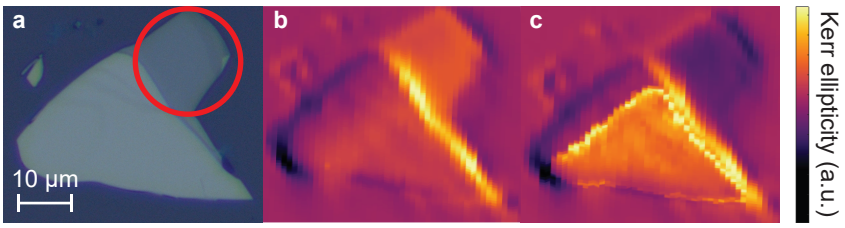

Figure 4.3: (a) A microscope image of the investigated FGT flake from batch I, obtained with a Zeiss Axio Scope.A1 microscope. The red encircled region was used for MOKE measurements. (b-c) Magnetic remanence scans obtained at $T = 79\,\mathrm{K}$ by measuring the Kerr ellipticity after an applied field of (b) $300\,\mathrm{mT}$ and (c) $-300\,\mathrm{mT}$ under an angle of 13° with respect to the in-plane axis. A 735 nm laser with a FWHM spot size of $\sim 3.5\,\mu\mathrm{m}$ was scanned across the flake to locally measure the Kerr ellipticity.

scanning the probe beam across the sample, and measuring the Kerr ellipticity ϵ at each position.

Considering the magnetization is uniform across the thin part of the flake and switches sign after applying positive and negative fields, the thin part of the flake forms a seemingly uniform magnetic domain that can be switched by applying a magnetic field. An example of a hysteresis loop measured within this magnetic domain is shown in the inset of Figure 4.4, revealing a sharp, single switch and a remanent net magnetization at $H = 0$, both associated with the hard, SD phase of FGT as discussed in section 2.2.2.

Since the easy axis lies along the c-direction of FGT, the magnetization is expected to be out-of-plane. This is verified by measuring the coercive field as a function of field angle, for which the result is shown in Figure 4.4. The coercive field was determined from the horizontal offset of an error function fitted through one of the steps of a hysteresis loop, as indicated by the fitted dashed line in the inset of Figure 4.4. If the magnetization is OOP, the coercive field should scale with the OOP component of the applied field[2]. The relation $H_C = H/\sin(\phi)$ follows, where H_C is the coercive field, H is the applied field and ϕ is the angle under which the field is applied. Fitting this relation, including an offset ϕ_0 to account for misaligning, yields the dashed line in Figure 4.4 and indeed confirms that the magnetization points, at least approximately, OOP, with $\phi_0 = 2.7 \pm 0.2°$.

Further measurements were performed on a flake from batch II, for which a microscope image is shown in Figure 4.5a and its remanence scans in Figure 4.5b-c. The red encircled domain appears uniform and will be used for further investigations.

Hysteresis loops were measured inside the uniform domain after ZFC for which the result is shown in Figure 4.6a. The three loops shown were measured consecutively in a time interval < 10 minutes and its features are discussed as follows. First, the switching behavior is sharp, indicating a hard switch of a single, uniformly magnetized magnetic domain as follows from section 2.2.2. All loops also show consistent plateaus for up and down magnetization at high

[2]Assuming a negligible contribution of the in-plane field component to the coercive behavior.

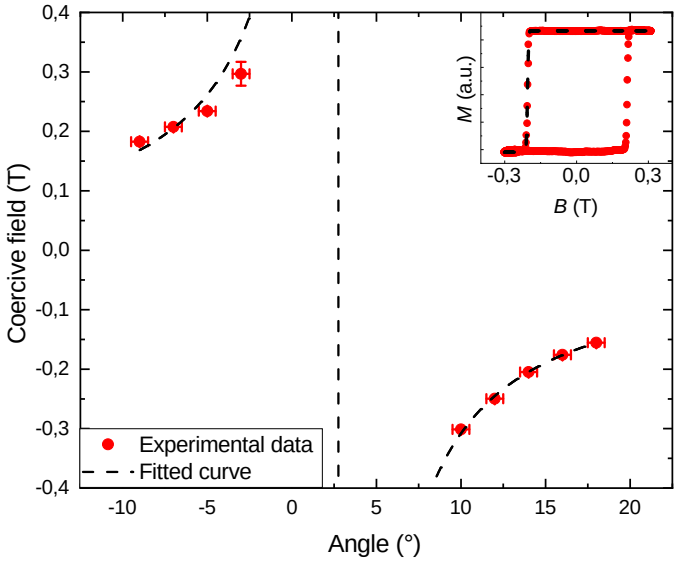

Figure 4.4: The coercive field plotted as a function of the angle under which the magnetic field is applied, with the relation $H_C = H/\sin(\phi)$ fitted by the dashed line. The inset shows a typical hysteresis loop ($\phi = 14°$), where an error function is fitted to determine the coercive field. All data was obtained at $T = 79\,\mathrm{K}$ by using a 735 nm laser.

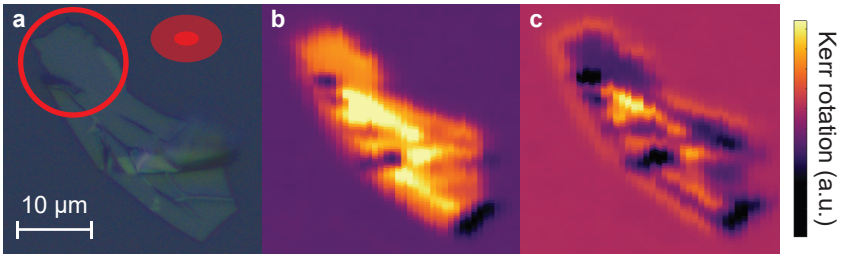

Figure 4.5: (a) A microscope image of the investigated FGT flake from batch II, obtained with a Zeiss Axio Scope.A1 microscope. The red encircled region indicates the investigated domain. The red semi-transparent and opaque ellipses respectively denote typical pump and probe spot sizes during a pump-probe experiment. (b-c) Magnetic remanence scans obtained at $T = 79\,\mathrm{K}$ by measuring the Kerr rotation after an applied field of (b) 300 mT and (c) $-300\,\mathrm{mT}$ under an angle of 13° with respect to the in-plane axis. A 735 nm laser with FWHM spot size of $2.9\,\mu\mathrm{m} \times 1.7\,\mu\mathrm{m}$ (horizontal × vertical directions) was scanned across the flake to locally measure the Kerr rotation.

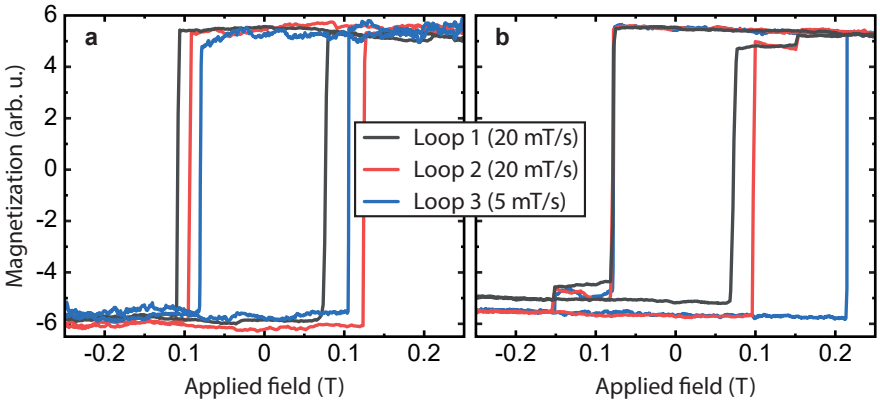

Figure 4.6: (a) Hysteresis loops measured with MOKE after (a) ZFC and (b) FC, the magnetization is obtained by measuring the Kerr rotation θ. The loops in each graph were measured consecutively within a 10 minute time period. FC was performed with an applied field under an angle of 17° with respect to the plane.

fields, further indicating that all measurements portray the same, single magnetic domain. Second, all loops have a certain bias, i.e. they are asymmetric around zero field, and third, the shape of the loop is not consistent throughout independent measurements, the coercive field changes on both sides between each measured loop, even leading to a shift from negative to positive bias between the first and second loop.

The variable hysteric behavior as well as the apparent bias for positive or negative field is rather peculiar, but is most likely explained by considering the formation of magnetic domains within the flake. If any neighboring domains are present in the vicinity of the measured domain, those domains might exert an additional(effective) field on the measured domain, leading to a biased loop as a function of solely the applied field. Indeed, already in the remanence scans displayed in Figures 4.5b-c domain formation manifests itself, showing that the magnetization is not uniform across the entire flake. Different parts of the flake, separated by cracks or differences in thickness, appear to have different magnetization. Moreover, in some parts the magnetization does not switch after the application of opposite magnetic fields, indicating a variable coercive field for different magnetic domains.

In addition to domain formation in the plane of the flake, domain formation might also occur along the *c*-direction, as is also observed in other VdW ferromagnets such as CrI_3 [113]. An example of such a configuration is illustrated in Figure 4.7, where one layer forms an up domain and two layers form a down domain. The domain boundary would typically form around structural defects, for example induced by slight oxidation of the flake [89]. Now, if one of the domains remain unperturbed by the applied magnetic field, for example because its coercive field exceeds the applied field, this domain will exert a bias on the switching of domains above or below the unperturbed domain.

Lastly, even though the measured part of the flake is thin, the formation of flux closure domains as discussed for bulk FGT in section 2.2.1 might still play

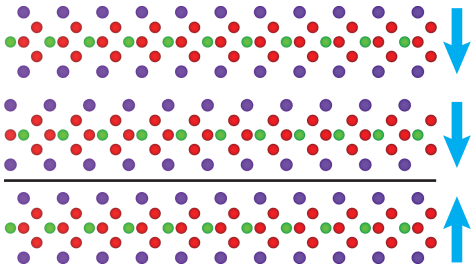

Figure 4.7: Configuration for possible layered magnetism in FGT, the blue arrows denote the magnetization direction of each layer.

a role, complicating the magnetic domain structure. Comparing the shape of the hysteresis loop to the hysteresis loops depicted in Figure 2.8a-b from section 2.2.2 indicates no formation of large-scale magnetic domains, so only the formation of surface flux closure domains such as the spike or double-walled domain from section 2.2.1 might contribute towards the variable hysteric behavior.

Following the results for ZFC and the hypothesis of domain formation influencing the hysteric behavior, the FC case was studied as well. As described in section 2.2.1, FC suppresses domain formation and generally leads to more uniform magnetic domains, which may lead to more stable and uniform hysteric behavior.

The resulting hysteresis loops measured after FC under a field of +250 mT under an angle of 17° are shown in Figure 4.6. The first loop was measured directly after FC, yielding a symmetric two-step switch. However, additional loops measured consecutively after the first loop show that on the positive field side, the loop evolves to a single-step switch, while on the negative field side the loop remains identical. After the third loop, the hysteresis loop remained stable for the rest of the measurements over a time period of at least multiple days.

The two-step switch indicates the presence of two magnetic domains with different coercive fields, confirming the hypothesis that domain formation plays a role in the magnetostatic behavior. Furthermore, the initial stabilization of the hysteresis loops is probably induced by the applied magnetic field during measurements and the asymmetric shape of the loop might be due to a more complicated domain structure surrounding the measured domain.

A possible explanation for the source of the domain formation might be found when considering the earlier discussed EDX results, indicating variations of iron content throughout the crystal. It has been shown earlier that the iron content has a large effect on the magnetic anisotropy in FGT [41] and therefore, a local variation in iron content would yield a local variation in anisotropy. The border of regions with different anisotropy could then act as a domain wall [114] and induce domain formation. However, EDX was only performed on typical length scales of tens of nanometers, so higher resolution measurements would be necessary to test this hypothesis.

Overall, more conclusive experimental evidence would be necessary for a proper conclusion regarding the source of domain formation, as well as to investigate along which direction(s) the domains form. As for now, the main takeaway from the static analysis emphasizes the importance of FC for more consistent magnetostatic behavior and the apparent formation of magnetic domains.

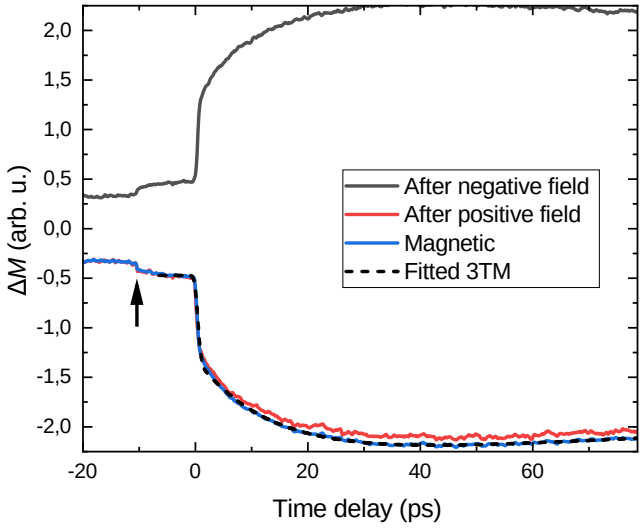

Figure 4.8: A typical result of a demagnetization measurement, conducted at $T = 79\,\mathrm{K}$ with a laser fluence of $26\,\mathrm{mJ\,cm^{-2}}$. The magnetic signal is obtained by subtracting the positive field curve from the negative field curve and dividing by two. The dashed curve illustrates the fitted 3TM model with a modified version of equation 2.19, as described in the main text. The wavelength of both the pump and probe pulse was 735 nm, and the pump and probe FWHM spot size were $9.6\,\mu\mathrm{m} \times 6.6\,\mu\mathrm{m}$ and $3.3\,\mu\mathrm{m} \times 2.0\,\mu\mathrm{m}$., respectively

4.3 Time-resolved measurements on thin FGT

Finally, time-resolved measurements were performed using the pump-probe technique discussed in section 3.3.3. All time-resolved measurements were performed on the earlier discussed flake from batch II, which is also shown in Figure 4.5a. A typical demagnetization curve is shown in Figure 4.8, where the magnetic signal is obtained as discussed in section 3.3.3 by subtracting the negative field signal from the positive field signal and dividing by two. The characteristic details of the demagnetization curve will be discussed in the following.

First, it is observed that the demagnetization curve resembles the profile of type II dynamics (see section 2.3), which indicates relatively fast thermal relaxation between the electron and phonon system compared to a slower thermal relaxation of the spin system, i.e. $\tau_E < \tau_M$.

Furthermore, after the arrival of each pump pulse, the pumped region of the flake will slowly cool down by conducting heat away to the rest of the flake and the substrate, which causes the slightly declining tail at the end of the signal. This process typically occurs at much larger timescales compared to relaxation between the various subsystems and can therefore only be really visually distinguished after internal relaxation between thermodynamic subsystems. In addition, due to the long diffusion timescale, some heat remains when the next pump pulse arrives. This results in an average heating of the pumped region, which shows up as the vertical offset in opposite direction for the negative and positive field curves.

Finally, a small bump is observed before arrival of the pump pulse, denoted

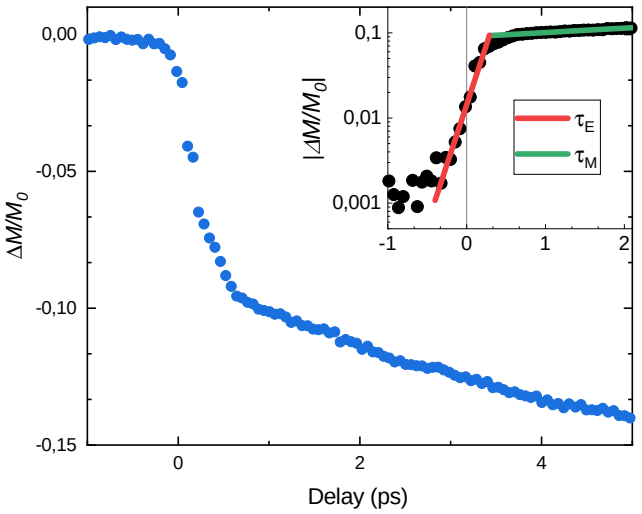

Figure 4.9: A detailed measurement of the first few picoseconds from the curve shown in Figure 4.8. The blue and black circles correspond to the same data set, plotted on a linear (blue) and logarithmic (black) scale. The logarithmic plot allows for clear visual distinction of the two timescales τ_E and τ_M, as illustrated by the red and green curves respectively.

by the arrow in Figure 4.8. This bump occurs due to the generation of secondary pump and probe paths by internal reflections of optical components in their respective paths. Due to these internal reflections, the path becomes slightly larger, which induces a relative delay between the main and secondary paths. The specific bump observed in front of the main signal follows from a secondary probe pulse measuring the effects induced by the main pump pulse. One might expect a similar bump on the opposite side of $t = 0$, induced by the main probe pulse measuring a secondary pump pulse. However, the energy of the secondary pump pulse is probably too small to excite any distinguishable dynamics compared to the dynamics excited by the main pump pulse.

The demagnetization curve from Figure 4.8 can also be normalized to obtain the relative amount of demagnetization. Such normalization can be achieved by measuring the step size of a hysteresis loop at time delays before and after arrival of the pump pulse as discussed in section 3.3.3. Normalization yields a maximum demagnetization of $15 \pm 2\,\%$ for the curve shown in Figure 4.8, for which the result is illustrated by the 90 K curve in Figure 4.11. Normalization was performed using the step size of a hysteresis loop measured at a delay of -6 ps as maximum magnetization, so the bump and average heating were excluded from normalization and only the effect induced by the pump pulse was taken into account.

To obtain more details on the demagnetization process, a modified version of the earlier obtained analytical solution of the 3TM model from equation 2.19 can be fitted through the demagnetization curve. The original equation is modified to account for heat diffusion by replacing ΔT_1 by $\Delta T_1/\sqrt{t/\tau_0 + 1}$. The resulting equation is then convoluted with the Gaussian probe pulse $\Gamma(t, \sigma) = \exp\left(-t^2/\sigma^2\right)/\sigma\sqrt{\pi}$, providing a relation that can be fitted through the demag-

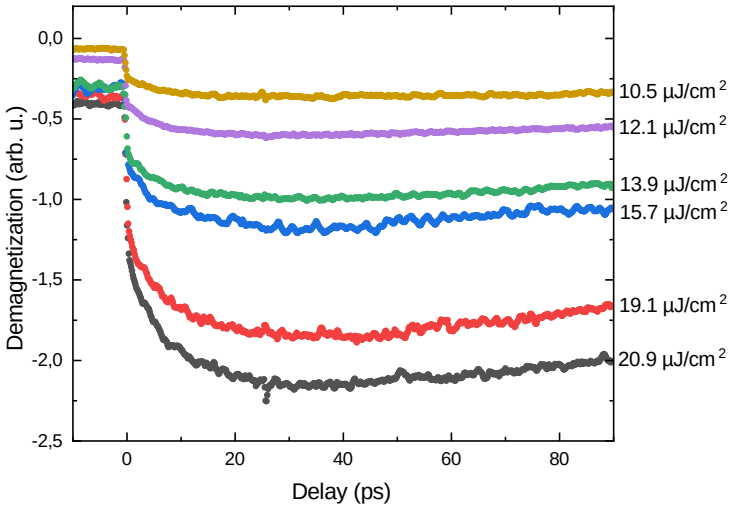

Figure 4.10: Demagnetization in FGT measured as a function of laser fluence. All measurements were performed at $T = 79\,\mathrm{K}$. The wavelength of both the pump and probe pulse was 735 nm, and the pump and probe FWHM spot size were $12\,\mu\mathrm{m} \times 6.5\,\mu\mathrm{m}$ and $2.9\,\mu\mathrm{m} \times 1.7\,\mu\mathrm{m}$., respectively

netization curve. The resulting fit is shown by the dashed line in Figure 4.8, and its derived parameters yield two distinct timescales $\tau_E = 0.20 \pm 0.01\,\mathrm{ps}$ and $\tau_M = 13.6 \pm 0.3\,\mathrm{ps}$, giving $\tau_E < \tau_M$, which is in line with the earlier hypothesized type II dynamics, although it is noted that the timescale τ_M is slightly larger when compared to other $3d$ ferromagnets such as nickel [50, 61, 85] and CoPt [84].

The presence of two distinct timescales can also be visually distinguished when zooming in on the first few picoseconds of the demagnetization curve, as shown in Figure 4.9. In the inset, the absolute value of the same data is plotted on a logarithmic scale and two distinct timescales manifest themselves as illustrated by the red (τ_E) and green (τ_M) curves.

Additional insight in the ultrafast magnetization dynamics of FGT can be obtained by measuring the demagnetization as a function of laser fluence. The respective demagnetization curves are shown in Figure 4.10, constituting two qualitative observations. First, the amount of demagnetization increases with pump fluence, as expected due to the larger amount of heat being injected in the system and thus leading to an increased amount of demagnetization. Furthermore, the length of the magnetic timescale seemingly decreases with decreasing fluence, which is also in correspondence with the microscopic three-temperature model as discussed in section 2.3.2.

Unfortunately, proper fitting was increasingly difficult as fluence decreases, which is due to the loss of distinct features for decreasing fluence. Therefore, the lower fluence curves could not be properly fitted and a more quantitative comparison remains unresolved, although the qualitative behavior is seemingly in line with predictions from the (M)3TM models. For future work, it is suggested to implement additional experimental measures to decrease the amount of fitting parameters and thus achieve increased fit quality.

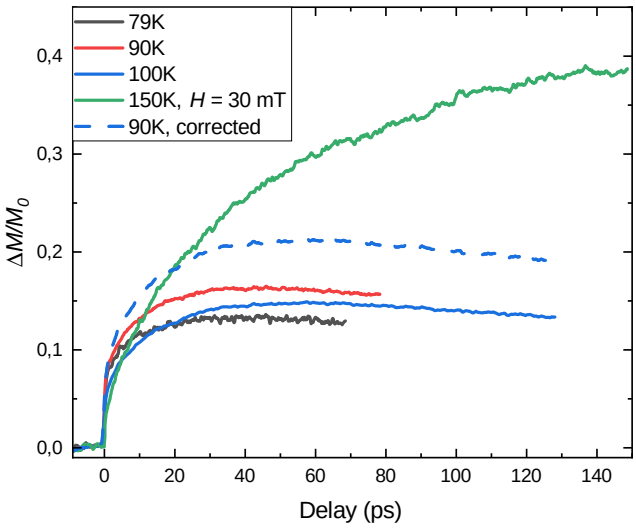

Figure 4.11: The normalized demagnetization curves measured at various temperatures. At 150 K, the pump pulse completely demagnetizes the sample, leading to the formation of a multi-domain state. In order to remagnetize the sample in-between pulses, a small field of 30 mT was applied under an angle of 17°. Normalization of the 150 K was performed by using the average normalization factor obtained from the other three curves and is therefore subject to a larger error.

In addition, the dynamic behavior was studied as a function of temperature. Taking into account the account the fluence-dependent results, a sufficiently high fluence of 25.7 µJ cm^{-2} was used to preserve the distinct features of the demagnetization curve. The respective curves are shown in Figure 4.11 and their characteristic features are discussed in the following.

First, the amount of demagnetization measured at 100 K does not seem to be in line with the 'expected' data when compared to the other three curves. The other curves show a consistent increase in amount of demagnetization as the temperature raises, but the 100 K curve reaches only slightly above the 79 K curve and stays well above the 90 K curve. This apparent deviation most likely follows from experimental factors, rather than intrinsic behavior of FGT.

More specifically, the change is most likely due to the probe beam being aligned to slightly different parts of the flake, caused by contractions and extensions of the sample holder due to thermal fluctuations. Such deviations are estimated to be limited to mostly a few micrometers. Still, the single-domain part of the flake is only a few micrometers larger compared to the full width at half maximum (FWHM) size of the probe beam, for which a typical size is indicated by the opaque ellipse in Figure 4.5a. Therefore, even a small misalignment of only a few micrometers could cause part of the probe beam to be incident on e.g. the substrate instead of the single-domain region. In this case, the demagnetization appears to be smaller due to the probe reflecting of a smaller part of the flake. Based on hysteresis loop step sizes, an estimate can be made of the actual relative position of this curve, which is indicated by the dashed curve in Figure 4.11.

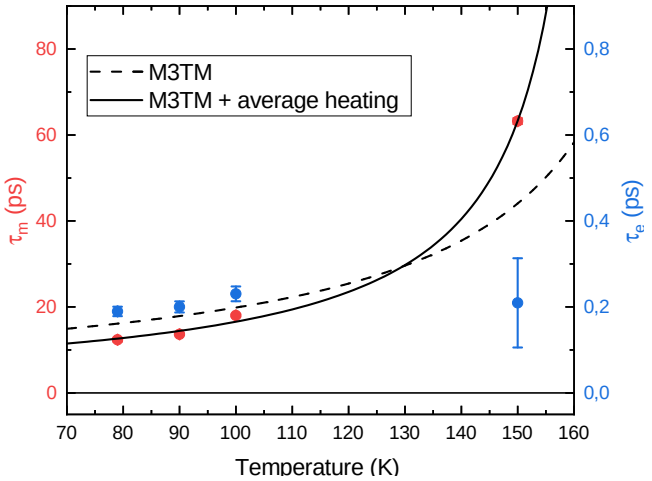

Figure 4.12: The evolution of the two characteristic timescales τ_E and τ_M as a function of temperature. Relation 2.21 is fitted through the τ_M data points, both with (dashed line) and without (solid line) including a horizontal offset to account for the average heating effect. Error bars are obtained using the standard error of the fit.

Fortunately, besides the influence on the apparent amount of demagnetization, other parameters such as the characteristic timescales will remain relatively unaffected. This is due to the pump beam being considerably larger than the probe beam, which is visualized in Figure 4.5a where the typical pump (probe) beam size during a pump-probe experiment is indicated by the semi-transparent (opaque) ellipse. As a result, the pump intensity is approximately uniform over the smaller probed region, leaving the characteristic timescales of the demagnetization process relatively unaffected.

Indeed, having a closer look at Figure 4.11 already hints that towards T_C, the characteristic timescale τ_M timescale increases consistently, as also expected from theory and earlier measurements on other $3d$-band ferromagnets [61, 85]. To achieve a more quantitative comparison, both timescales were extracted again by fitting the earlier described modified version of equation 2.19, for which the results are plotted as a function of temperature in Figure 4.12.

As follows, τ_M indeed increases as the temperature approaches T_C, while τ_E remains relatively constant, which is in line with M3TM predictions [61]. Furthermore, equation 2.21 can be used to fit the magnetic timescale as a function of temperature. However, using the equation in its bare form does not result in a proper fit through the data, as indicated by the dashed line in Figure 4.12. This discrepancy might be explained by considering that equation 2.21 does not account for the earlier observed average heating effect, which is due to the pumped region not cooling down entirely in-between pulses.

In a simple approximation, the increase in temperature due to average heating depends solely on the average power of the pump beam, which is constant over the various temperature measurements. Therefore, the average heating effect can be accounted for by replacing the temperature in equation 2.21 by $T_{\text{eff}} = T + \Delta T_{\text{avg}}$, where ΔT_{avg} is the increase in temperature due to average

heating and is used as an additional fitting parameter. The resulting fitted curve fits reasonably well as illustrated by the solid line in Figure 4.12, yielding $\Delta T_{avg} = 23 \pm 1\,\mathrm{K}$.

This temperature difference can also be estimated based on the step size of hysteresis loops following a similar procedure as for the curve normalization described in section 3.3.3. A first hysteresis loop was measured with the pump beam blocked, meaning that the magnetization is probed in absence of average heating. A second hysteresis loop was subsequently measured while pumping the sample, but at a time delay $t < 0$, i.e. before arrival of the pump pulse. In this way, the impact of average heating on the magnetization is measured.

The relative difference in magnetization due to average heating can then be compared to the experimentally obtained M, T-curve for bulk FGT as shown in Figure 4.1, for which a third order polynomial was fitted between 75 K and 130 K to determine the magnetization as a function of temperature in this regime. This function is then used to determine the temperature difference induced by average heating, yielding $\Delta T_{avg} = 16 \pm 7\,\mathrm{K}$, which is in reasonable correspondence with the value obtained from fitting τ_M.

Furthermore, the material-dependent constant $R = 0.085 \pm 0.005\,\mathrm{ps}^{-1}$ is obtained from fitting τ_M as a function of T, which is compared to the electron-phonon relaxation rate to determine the dominant demagnetization process as is described in section 2.3.2. $1/\tau_{E0}$ can be estimated by taking its value close to T_C, for which the value obtained at 150 K will be used, yielding $1/\tau_{E0} \approx 5 \pm 2\,\mathrm{ps}^{-1}$. Comparing this to R yields $R \ll 1/\tau_{E0}$, meaning that the demagnetization process will be dominantly of type II in accordance with the observed behavior.

These results conclude the time-resolved investigations, which mainly revolve around the first measurement of ultrafast demagnetization in a Van der Waals material. The dynamics of the demagnetization process were furthermore qualitatively studied as a function laser fluence and quantitatively as a function of temperature. The demagnetization was characterized to be of type II and its characteristic behavior as a function of fluence and temperature is in well agreement with the previously developed 3TM and M3TM models, as well as with earlier measurements on other $3d$-band ferromagnets.

Chapter 5

Conclusion and outlook

To conclude, the main result obtained in this thesis features the first observation of ultrafast demagnetization in a ferromagnetic Van der Waals material, being Fe_3GeTe_2, and a temperature-dependent study of the timescales involved in this demagnetization process. Furthermore, a static study on both bulk and thin FGT was performed. The conclusions and outlook regarding both results will be discussed in more detail below.

5.1 Static measurements

SQUID investigations of bulk FGT crystals yielded a slightly lower Curie temperature compared to its literature value. In earlier works, a similar decrease was observed and related to an iron-deficiency in the crystal. This result was confirmed by performing EDX on the crystal, indeed yielding an overall iron-deficiency of the sample. Additionally, the iron deficiency was found to vary on length scales of tens of micrometers between 0 and 10 percent. Since measurements were not performed on smaller length scales, more local variations cannot be excluded and should be investigated in future experiments.

Furthermore, the magnetostatic behavior of thin FGT flakes was investigated using MOKE. Hysteresis loops for both zero-field-cooling and field-cooling were measured, yielding various peculiar observations. In the ZFC case, hysteresis loops were shown to have a field bias up to tens of milliteslas and inconsistent coercive fields over various measurements. Furthermore, for the FC case a two-step switch was observed, which after a few loops stabilizes towards a consistent, but asymmetric shape of the hysteresis loop. The two-step switch remained for negative field, while for positive field it was replaced by a single-step switch with slightly higher overall coercivity. It is furthermore suspected that FC suppresses the formation of more complicated domain structures.

Still, a more in-depth study of the magneto-static behavior would be needed for drawing proper conclusions. It remains for example unclear whether the domains form along the (out-of-plane) c-direction or in the ab-plane and what the mechanisms are behind domain formation, as well as what the mechanisms are behind the asymmetric switching in the FC case and irregular coercive fields in the ZFC case.

More insight in the magnetostatic behavior and domain formation can be

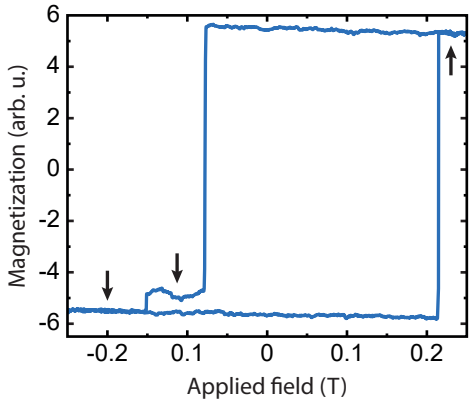

Figure 5.1: The stable ZFC hysteresis loop as isolated from Figure 4.6b. The arrows indicate possible field values where it would be interesting to perform spatial domain mapping of the flake.

obtained by spatially mapping the magnetic domains for various fields corresponding to different plateaus in the hysteresis loop, as indicated by the arrows in Figure 5.1. Mapping in the *ab*-plane can be performed using MOKE and various other techniques; magnetic force microscopy (MFM) to increase the spatial resolution and scanning electron microscopy with polarization analysis (SEMPA) to investigate the chirality of more complicated domain patterns. Complex MOKE [61, 102] can be used as an initial approach to spatial mapping along the *c*-direction.

Furthermore, EDX can be used for micrometer-scale mapping of the iron deficiency in both bulk and thin FGT, for which the results can be compared with spatial maps of the magnetization obtained by the earlier mentioned techniques. Such investigations might lead to more insight in the influence of iron deficiencies on the magnetic behavior of the material. It has for example been observed in earlier work that the anisotropy strongly depends on the Fe content [41], which would lead to local variations of the anisotropy for a spatially varying iron deficiency. Such local variations might be one of the mechanisms behind the domain formation in thin FGT. Moreover, measuring and controlling such local anisotropy variations is of potential use in spintronic memory devices and logic circuits [114–116].

5.2 Time-resolved measurements

Subsequently, time-resolved measurements were performed yielding the observation of ultrafast magnetization dynamics in FGT. It has been found that the demagnetization profile is of type II across all measurements, which is confirmed by comparing typical values of the magnetic timescale $\tau_M = 13.6 \pm 0.3\,\text{ps}$ to typical values obtained for the electron-phonon relaxation timescale $\tau_E = 0.20 \pm 0.01\,\text{ps}$, yielding $\tau_E < \tau_M$. It is also noted that the magnetic timescale τ_M is relatively long when compared to other transition metal ferromagnets.

The evolution of these timescales was studied qualitatively as a function laser fluence and quantitatively as a function of temperature, and it was found that in

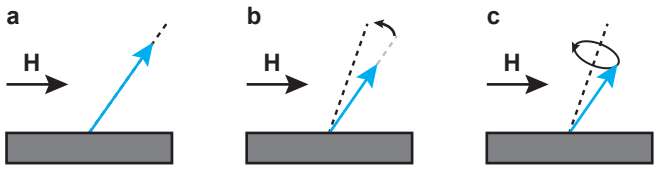

Figure 5.2: An illustration of how precession can be induced using a ferromagnet with out-of-plane anisotropy and an in-plane applied field. (a) First the applied field H cants the magnetization (blue) towards a new equilibrium (dashed line), (b) ultrafast heating by a laser pulse quenches the magnetization and changes the anisotropy, resulting in a new equilibrium axis and (c) due to LLG dynamics, the magnetization will precess around its new equilibrium value.

both cases the behavior corresponds well with the (microscopic) three temperature model and earlier results obtained in other transition metal ferromagnets. More specifically, it was found that the magnetic timescale diverges as T approaches T_C, as expected from the M3TM. This temperature dependence was fitted, while accounting for average heating, returning a value for the material-specific constant $R = 0.085 \pm 0.005\,\mathrm{ps}^{-1}$. Comparing R to the electron-phonon relaxation timescale close to the Curie temperature then gives $R << 1/\tau_{E0}$, indicating type II magnetization is dominant in FGT, in correspondence with earlier qualitative and quantitative observations.

Building onto the results obtained in this work, additional fluence and temperature dependent studies can be conducted on FGT to provide more insight in its ultrafast magnetic behavior. Moreover, such a study would be of particular interest for few-layer FGT, in the thickness region where the transition from bulk to two-dimensional magnetism occurs. Due to this transition, the critical exponent β will change, leading to different temperature-dependent behavior of the magnetization.

It is therefore expected that different magnetization dynamics arise between the two-dimensional phase in monolayer FGT, the crossover phase in 2-5 layer FGT and the bulk phase in > 5 layer FGT, which would lead to a thickness-dependent demagnetization process. Consequentially, the demagnetization process can be investigated across various dimensions in a single material. Comparing such investigations with existing microscopic models may lead to increased fundamental understanding of the microscopic mechanisms behind ultrafast demagnetization.

Another possible extension to this work is investigating coherent spin waves excited by a pump pulse. For this, a magnetic field can be applied along the in-plane direction in the *ab*-plane. Initially, this magnetic field will slightly cant the equilibrium orientation of the macroscopic magnetization, as depicted in Figure 5.2a. Now, a pump pulse is used to raise the local temperature, not only leading to quenching of the magnetization but also changing the temperature-dependent magnetic anisotropy [45, 62]. Therefore, a new equilibrium position arises as shown in Figure 5.2b, after which the magnetization starts to precess around the new equilibrium position according to the Laundau-Lifshiftz-Gilbert (LLG) dynamics [117, 118], as depicted in Figure 5.2c. This precession can be measured with the probe pulse and is equivalent to its ferromagnetic resonance [62, 119], which is useful for studying the magnetic anisotropy in FGT, as well as

some dynamic phenomena such as its Gilbert damping factor and field-assisted switching.

FGT can also be used in VdW heterostructures, where the ultrafast magnetization dynamics can be exploited for e.g. spin current injection in other VdW materials [19, 57, 120, 121] or excitation of terahertz spin waves [67–69], for example by combining Fe_3GeTe_2 with the in-plane ferromagnet Fe_4GeTe_2 [122].

To summarize, the results obtained in this work open up possibilities for combining femtomagnetism with Van der Waals materials, two fields that have been highlighted individually for their impact on spintronics. It has been found that the Van der Waals ferromagnet Fe_3GeTe_2 exhibits ultrafast demagnetization of type II and behaves in corresponding with existent models of ultrafast magnetization dynamics. This work provides the basis for more detailed investigation of ultrafast magnetization dynamics in FGT, which has potential applications in Van der Waals spintronics and could lead to increased fundamental insight in the microscopic mechanisms behind the ultrafast demagnetization process.

References

[1] K. S. Novoselov, A. K. Geim, S. V. Morozov, D. Jiang, Y. Zhang, S. V. Dubonos, I. V. Grigorieva, and A. A. Firsov, "Electric field effect in atomically thin carbon films", Science **306**, 666–669 (2004).

[2] A. H. Castro Neto, F. Guinea, N. M. R. Peres, K. S. Novoselov, and A. K. Geim, "The electronic properties of graphene", Rev. Mod. Phys. **81**, 109–162 (2009).

[3] S. Z. Butler et al., "Progress, challenges, and opportunities in two-dimensional materials beyond graphene", ACS Nano **7**, 2898–2926 (2013).

[4] K. S. Novoselov, A. K. Geim, S. V. Morozov, D. Jiang, M. I. Katsnelson, I. V. Grigorieva, S. V. Dubonos, and A. A. Firsov, "Two-dimensional gas of massless Dirac fermions in graphene", Nature **438**, 197 (2005).

[5] A. Splendiani, L. Sun, Y. Zhang, T. Li, J. Kim, C. Chim, G. Galli, and F. Wang, "Emerging photoluminescence in monolayer MoS_2", Nano Lett. **10**, 1271–1275 (2010).

[6] K. F. Mak, C. Lee, J. Hone, J. Shan, and T. F. Heinz, "Atomically thin MoS_2: A new direct-gap semiconductor", Phys. Rev. Lett. **105**, 136805 (2010).

[7] A. K. Geim, "Graphene: status and prospects", Science **324**, 1530–1534 (2009).

[8] The Royal Swedish Academy of Sciences, *The Nobel Prize in Physics 2010*, Press Release, (Oct. 2010) `https://www.nobelprize.org/uploads/2018/06/press-9.pdf` (visited on 01/16/2020).

[9] Y. Liu, N. O. Weiss, X. Duan, H. Cheng, Y. Huang, and X. Duan, "Van der Waals heterostructures and devices", Nat. Rev. Mater. **1**, 16042 (2016).

[10] A. K. Geim and I. V. Grigorieva, "Van der Waals heterostructures", Nature **499**, 419–425 (2013).

[11] K. S. Novoselov, D. Jiang, F. Schedin, T. J. Booth, V. V. Khotkevich, S. V. Morozov, and A. K. Geim, "Two-dimensional atomic crystals", Proc. Natl. Acad. Sci. U.S.A. **102**, 10451–10453 (2005).

[12] A. C. Ferrari et al., "Science and technology roadmap for graphene, related two-dimensional crystals, and hybrid systems", Nanoscale **7**, 4598–4810 (2015).

[13] K. S. Novoselov, A. Mischchenko, A. Carvalho, and A. H. Castro Neto, "2D materials and Van der Waals heterostructures", Science **353**, aac9439 (2016).

[14] L. J. Li, E. C. T. O'Farrell, K. P. Loh, G. Eda, B. Özyilmaz, and A. H. Castro Neto, "Controlling many-body states by the electric-field effect in a two-dimensional material", Nature **529**, 185–189 (2016).

[15] Y. Cao, V. Fatemi, S. Fang, K. Watanabe, T. Taniguchi, E. Kaxiras, and P. Jarillo-Herrero, "Unconventional superconductivity in magic-angle graphene superlattices", Nature **556**, 43–50 (2018).

[16] Z. Y. Rong and P. Kuiper, "Electronic effects in scanning tunneling microscopy: Moiré pattern on a graphite surface", Phys. Rev. B **48**, 17427–17431 (1993).

[17] R. Bistritzer and A. H. MacDonald, "Moiré bands in twisted double-layer graphene", Proc. Natl. Acad. Sci. U.S.A. **108**, 12233–12237 (2011).

[18] C. R. Woods et al., "Commensurate–incommensurate transition in graphene on hexagonal boron nitride", Nat. Phys. **10**, 451–456 (2014).

[19] H. Wei, R. K. Kawakami, M. Gmitra, and J. Fabian, "Graphene spintronics", Nat. Nanotechnol. **9**, 794–807 (2014).

[20] M. Gmitra and J. Fabian, "Graphene on transition-metal dichalcogenides: A platform for proximity spin-orbit physics and optospintronics", Phys. Rev. B **92**, 155403 (2015).

[21] S. Manzeli, D. Ovchinnikov, D. Pasquier, O. V. Yazyev, and A. Kis, "2D transition metal dichalcogenides", Nat. Rev. Mater. **2**, 17033 (2017).

[22] J. Park, "Opportunities and challenges of 2D magnetic Van der Waals materials: magnetic graphene?", J. Phys. Condens. Matter **28**, 301001 (2016).

[23] K. S. Burch, D. Mandrus, and J. Park, "Magnetism in two-dimensional Van der Waals materials", Nature **563**, 47–52 (2018).

[24] C. Gong and X. Zhang, "Two-dimensional magnetic crystals and emergent heterostructure devices", Science **363**, eaav4450 (2019).

[25] M. Gibertini, M. Koperski, A. F. Morpurgo, and K. S. Novoselov, "Magnetic 2D materials and heterostructures", Nat. Nanotechnol. **14**, 408–419 (2019).

[26] S. A. Wolf, D. D. Awschalom, R. A. Buhrman, J. M. Daughton, S. von Molnár, M. L. Roukes, A. Y. Chtchelkanova, and D. M. Treger, "Spintronics: A spin-based electronics vision for the future", Science **294**, 1488–1495 (2001).

[27] A. Kirilyuk, A. V. Kimel, and T. Rasing, "Ultrafast optical manipulation of magnetic order", Rev. Mod. Phys. **82**, 2731–2784 (2010).

[28] T. Jungwirth, X. Marti, P. Wadley, and J. Wunderlich, "Antiferromagnetic spintronics", Nat. Nanotechnol. **11**, 231–241 (2016).

[29] V. Baltz, A. Manchon, M. Tsoi, T. Moriyama, T. Ono, and Y. Tserkovnyak, "Antiferromagnetic spintronics", Rev. Mod. Phys. **90**, 015005 (2018).

[30] P. Němec, M. Fiebig, T. Kampfrath, and A. V. Kimel, "Antiferromagnetic opto-spintronics", Nat. Phys. **14**, 229–241 (2018).

[31] L. A. Walsh and C. L. Hinkle, "Van der Waals epitaxy: 2D materials and topological insulators", Appl. Mater. Today **9**, 504–515 (2017).

[32] Y. Liu, Y. Huang, and X. Duan, "Van der Waals integration before and beyond two-dimensional materials", Nature **567**, 323–333 (2019).

[33] Z. Liu et al., "Ultrathin high-temperature oxidation-resistant coatings of hexagonal boron nitride", Nat. Commun. **4**, 2541 (2013).

[34] A. S. Mayorov, R. V. Gorbachev, S. V. Morozov, L. Britnell, R. Jalil, L. A. Ponomarenko, P. Blake, K. S. Novoselov, K. Watanabe, and T. Taniguchi, "Micrometer-scale ballistic transport in encapsulated graphene at room temperatur", Nano Lett. **11**, 2396–2399 (2011).

[35] N. D. Mermin and H. Wagner, "Absence of ferromagnetism or antiferromagnetism in one- or two-dimensional isotropic Heisenberg models", Phys. Rev. Lett. **17**, 1133–1136 (1966).

[36] P. C. Hohenberg, "Existence of long-range order in one and two dimensions", Phys. Rev. **158**, 383–386 (1967).

[37] E. Ising, "Beitrag zur theorie des ferromagnetismus", Z. Phys. **31**, 253–258 (1925).

[38] H. Deiseroth, K. Aleksandrov, C. Reiner, L. Kienle, and R. K. Kremer, "Fe_3GeTe_2 and Ni_3GeTe_2 – two new layered transition-metal compounds: crystal structures, HRTEM investigations, and magnetic and electrical properties", Eur. J. Inorg. Chem. **2006**, 1561–1567 (2006).

[39] B. Chen, J. Yang, H. Wang, M. Imai, H. Ohta, C. Michioka, K. Yoshimura, and M. Fang, "Magnetic properties of layered itinerant electron ferromagnet Fe_3GeTe_2", J. Phys. Soc. Jpn. **82**, 124711 (2013).

[40] J. Zhu et al., "Electronic correlation and magnetism in the ferromagnetic metal Fe_3GeTe_2", Phys. Rev. B **93**, 144404 (2016).

[41] A. F. May, S. Calder, C. Cantoni, H. Cao, and M. A. McGuire, "Magnetic structure and phase stability of the Van der Waals bonded ferromagnet Fe_3GeTe_2", Phys. Rev. B **93**, 014411 (2016).

[42] H. L. Zhuang, P. R. C. Kent, and R. G. Hennig, "Strong anisotropy and magnetostriction in the two-dimensional Stoner ferromagnet Fe_3GeTe_2", Phys. Rev. B **93**, 134407 (2016).

[43] Y. Wang, C. Xian, J. Wang, B. Liu, L. Ling, L. Zhang, L. Cao, Z. Qu, and Y. Xiong, "Anisotropic anomalous Hall effect in triangular itinerant ferromagnet Fe_3GeTe_2", Phys. Rev. B **96**, 134428 (2017).

[44] Z. Fei et al., "Two-dimensional itinerant ferromagnetism in atomically thin Fe_3GeTe_2", Nat. Mater. **17**, 778–782 (2018).

[45] C. Tan, J. Lee, S. Jung, T. Park, S. Albarakati, J. Partridge, M. R. Field, D. G. McCulloch, L. Wang, and C. Lee, "Hard magnetic properties in nanoflake Van der Waals Fe_3GeTe_2", Nat. Commun. **9**, 1554 (2018).

[46] N. León-Brito, E. D. Bauer, F. Ronning, J. D. Thompson, and R. Movshovich, "Magnetic microstructure and magnetic properties of uniaxial itinerant ferromagnet Fe_3GeTe_2", J. Appl. Phys. **120**, 083903 (2016).

[47] G. D. Nguyen, J. Lee, T. Berlijn, Q. Zou, S. M. Hus, J. Park, Z. Gai, C. Lee, and A. Li, "Visualization and manipulation of magnetic domains in the quasi-two-dimensional material Fe_3GeTe_2", Phys. Rev. B **97**, 014425 (2018).

[48] Q. Li et al., "Patterning-induced ferromagnetism of Fe_3GeTe_2 Van der Waals materials beyond room temperature", Nano Lett. **18**, 5974–5980 (2018).

[49] Y. Deng et al., "Gate-tunable room-temperature ferromagnetism in two-dimensional Fe_3GeTe_2", Nature **563**, 94–99 (2018).

[50] E. Beaurepaire, J. Merle, A. Daunois, and J. Bigot, "Ultrafast spin dynamics in ferromagnetic nickel", Phys. Rev. Lett. **76**, 4250–4253 (1996).

[51] M. van Kampen, "Ultrafast spin dynamics, In ferromagnetic metals", PhD thesis (2003).

[52] M. van Kampen, J. T. Kohlhepp, W. J. M. de Jonge, B. Koopmans, and R. Coehoorn, "Sub-picosecond electron and phonon dynamics in nickel", J. Phys. Condens. Matter **17**, 6823–6834 (2005).

[53] B. Koopmans, "Time-resolved Kerr-effect and spin dynamics in itinerant ferromagnets", in *Handbook of magnetism and advanced magnetic materials*, Vol. 3 (American Cancer Society, Dec. 2007).

[54] A. Vaterlaus, T. Beutler, and F. Meier, "Spin-lattice relaxation time of ferromagnetic gadolinium determined with time-resolved spin-polarized photoemission", Phys. Rev. Lett. **67**, 3314–3317 (1991).

[55] W. Hübner and K. H. Bennemann, "Simple theory for spin-lattice relaxation in metallic rare-earth ferromagnets", Phys. Rev. B **53**, 3422–3427 (1996).

[56] B. Koopmans, G. Malinowski, F. Dalla Longa, D. Steiauf, M. Fähnle, and T. Roth, "Explaining the paradoxical diversity of ultrafast laser-induced demagnetization", Nat. Mater. **9**, 259–265 (2010).

[57] M. Battiato, K. Carva, and P. M. Oppeneer, "Superdiffusive spin transport as a mechanism of ultrafast demagnetization", Phys. Rev. Lett. **105**, 027203 (2010).

[58] A. Eschenlohr, M. Battiato, P. Maldonado, N. Pontius, T. Kachel, K. Holldack, R. Mitzner, A. Föhlisch, P. M. Oppeneer, and C. Stamm, "Ultrafast spin transport as key to femtosecond demagnetization", Nat. Mater. **12**, 332–336 (2013).

[59] A. J. Schellekens, W. Verhoeven, T. N. Vader, and B. Koopmans, "Investigating the contribution of superdiffusive transport to ultrafast demagnetization of ferromagnetic thin films", Appl. Phys. Lett. **102**, 252408 (2013).

[60] F. Hellman et al., "Interface-induced phenomena in magnetism", Rev. Mod. Phys. **89**, 025006 (2017).

[61] A. J. Schellekens, "Manipulating spins, Novel methods for controlling magnetization dynamics on the ultimate timescale", PhD thesis (2014).

[62] M. van Kampen, C. Jozsa, J. T. Kohlhepp, P. LeClair, L. Lagae, W. J. M. de Jonge, and B. Koopmans, "All-optical probe of coherent spin waves", Phys. Rev. Lett. **88**, 227201 (2002).

[63] I. Radu et al., "Transient ferromagnetic-like state mediating ultrafast reversal of antiferromagnetically coupled spins", Nature **472**, 205–208 (2011).

[64] T. A. Ostler et al., "Ultrafast heating as a sufficient stimulus for magnetization reversal in a ferrimagnet", Nat. Commun. **3**, 666 (2012).

[65] C. D. Stanciu, F. Hansteen, A. V. Kimel, A. Kirilyuk, A. Tsukamoto, A. Itoh, and T. Rasing, "All-optical magnetic recording with circularly polarized light", Phys. Rev. Lett. **99**, 047601 (2007).

[66] C.-H. Lambert et al., "All-optical control of ferromagnetic thin films and nanostructures", Science **345**, 1337–1340 (2014).

[67] I. Razdolski, A. Alekhin, N. Ilin, J. P. Meyburg, V. Roddatis, D. Diesing, U. Bovensiepen, and A. Melnikov, "Nanoscale interface confinement of ultrafast spin transfer torque driving non-uniform spin dynamics", Nat. Commun. **8**, 15007 (2017).

[68] M. L. M. Lalieu, P. L. J. Helgers, and B. Koopmans, "Absorption and generation of femtosecond laser-pulse excited spin currents in noncollinear magnetic bilayers", Phys. Rev. B **96**, 014417 (2017).

[69] M. L. M. Lalieu, R. Lavrijsen, R. A. Duine, and B. Koopmans, "Investigating optically excited terahertz standing spin waves using noncollinear magnetic bilayers", Phys. Rev. B **99**, 184439 (2019).

[70] R. Peierls, "On Ising's model of ferromagnetism", Math. Proc. Camb. Philos. Soc. **32**, 477–481 (1936).

[71] L. Onsager, "Crystal Statistics. I. A two-dimensional model with an order-disorder transition", Phys. Rev., 2nd ser. **65**, 117–149 (1944).

[72] P. Weiss, "L'hypothèse du champ moléculaire et la propriété ferromagnétique", J. Phys. Theor. Appl., 4th ser. **6**, 661–690 (1907).

[73] J. M. D. Coey, *Magnetism and magnetic materials* (Cambridge University Press, 2010).

[74] N. Goldenfeld, *Lectures on phase transitions and the renormalization group* (CRC Press, 1992).

[75] V. L. Berezinskii, "Destruction of long-rang order in one-dimensional and two-dimensional systems having a continuous symmetry group. I. Classical systems.", J. Exp. Theor. Phys. **32**, 493–500 (1971).

[76] V. L. Berezinskii, "Destruction of long-range order in one-dimensional and two-dimensional systems possessing a continuous symmetry group. II. Quantum systems.", J. Exp. Theor. Phys. **34**, 610–616 (1971).

[77] J. M. Kosterlitz and D. J. Thouless, "Ordering, metastability and phase transitions in two-dimensional systems", J. Phys. C Solid State Phys. **6**, 1181–1203 (1973).

[78] M. T. Johnson, P. J. H. Bloemen, F. J. A. den Broeder, and J. J. de Vries, "Magnetic anisotropy in metallic multilayers", Rep. Prog. Phys. **59**, 1409–1458 (1996).

[79] V. Y. Verchenko, A. A. Tsirlin, A. V. Sobolev, I. A. Presniakov, and A. V. Shevelkov, "Ferromagnetic order, strong magnetocrystalline anisotropy, andmagnetocaloric effect in the layered telluride $Fe_{3-\delta}GeTe_2$", Inorg. Chem. **54**, 8598–8607 (2015).

[80] C. Kittel, "Physical theory of ferromagnetic domains", Rev. Mod. Phys. **21**, 541–583 (1949).

[81] C. Kittel, "Theory of the structure of ferromagnetic domains in films and small particles", Phys. Rev. **70**, 965–971 (1946).

[82] J. B. Goodenough, "Interpretation of domain patterns recently found in BiMn and SiFe alloys", Phys. Rev. **102**, 356–365 (1956).

[83] B. Liu, Y. Zou, S. Zhou, L. Zhang, Z. Wang, H. Li, Z. Qu, and Y. Zhang, "Critical behavior of the Van der Waals bonded high T_C ferromagnet Fe_3GeTe_2", Sci. Rep. **7**, 6184 (2017).

[84] F. Dalla Longa, "Laser-induced magnetization dynamics, An ultrafast journey among spins and light pulses", PhD thesis (2008).

[85] T. Roth, A. J. Schellekens, S. Alebrand, O. Schmitt, D. Steil, B. Koopmans, M. Cinchetti, and M. Aeschlimann, "Temperature dependence of laser-induced demagnetization in Ni: A key for identifying the underlying mechanism", Phys. Rev. X **2**, 021006 (2012).

[86] A. J. Schellekens and B. Koopmans, "Microscopic model for ultrafast magnetization dynamics of multisublattice magnets", Phys. Rev. B **87**, 020407 (2013).

[87] K. C. Kuiper, T. Roth, A. J. Schellekens, O. Schmitt, B. Koopmans, M. Cinchetti, and M. Aeschlimann, "Spin-orbit enhanced demagnetization rate in Co/Pt-multilayers", Appl. Phys. Lett. **105**, 202402 (2014).

[88] E. Turgut et al., "Controlling the competition between optically induced ultrafast spin-flip scattering and spin transport in magnetic multilayers", Phys. Rev. Lett. **110**, 197201 (2013).

[89] D. Kim et al., "Antiferromagnetic coupling of Van der Waals ferromagnetic Fe_3GeTe_2", Nanotechnology **30**, 245701 (2019).

[90] P. Blake, E. W. Hill, A. H. Castro Neto, K. S. Novoselov, D. Jiang, R. Yang, T. J. Booth, and A. K. Geim, "Making graphene visible", Appl. Phys. Lett. **91**, 063124 (2007).

[91] A. Castellanos-Gomez, N. Agraït, and G. Rubio-Bollinger, "Optical identification of atomically thin dichalcogenide crystals", Appl. Phys. Lett. **96**, 213116 (2010).

[92] M. Faraday, "I. Experimental researches in electricity. — nineteenth series", Phil. Trans. R. Soc. **136**, 1–20 (1846).

[93] M. E. Verdet, "Recherches sur les propriétés optiques développées dans les corps transparents par l'action du magnétisme", Ann. Chim. Phys., 3rd ser. **52**, 129–163 (1858).

[94] J. Kerr, "On rotation of the plane of polarization by reflection from the pole of a magnet", Philos. Mag. J. Sci., 5th ser. **3**, 321–343 (1877).

[95] C. You and S. Shin, "Derivation of simplified analytic formulae for magneto-optical Kerr effects", Appl. Phys. Lett. **69**, 1315–1317 (1996).

[96] S. C. P. van Kooten, "Optical manipulation of magnetism in EuSe", Internship Report (2019).

[97] P. Bruno, "Tight-binding approach to the orbital magnetic moment and magnetocrystalline anisotropy of transition-metal monolayers", Phys. Rev. B **39**, 865–868 (1989).

[98] R. W. Boyd, *Nonlinear optics*, 3rd ed. (Academic Press, 2008).

[99] S. C. P. van Kooten, P. A. Usachev, X. Gratens, A. R. Naupa, V. A. Chitta, G. Springholz, and A. B. Henriques, "Converting Faraday rotation into magnetization in europium chalcogenides", J. Appl. Phys. **126**, 095701 (2019).

[100] A. Sommerfeld, *Optics* (Academic Press, 1954).

[101] R. C. Jones, "A new calculus for the treatment of optical systems I. Description and discussion of the calculus", J. Opt. Soc. Am. **31**, 488–503 (1941).

[102] M. L. M. Lalieu, "Femtomagnetism meets spintronics and magnonics", PhD thesis (2019).

[103] D. Colton and R. Kress, *Inverse acoustic and electromagnetic scattering theory*, Applied Mathematical Sciences (Springer, 1998).

[104] B. D. Josephson, "Possible new effects in superconductive tunneling", Phys. Lett. **1**, 251–253 (1962).

[105] P. W. Anderson and J. M. Rowell, "Probable observation of the Josephson superconducting tunneling effect", Phys. Rev. Lett. **10**, 230–232 (1963).

[106] R. C. Jaklevic, J. Lambe, A. H. Silver, and J. E. Mercereau, "Quantum interference effects in Josephson tunneling", Phys. Rev. Lett. **12**, 159–160 (1964).

[107] R. P. Feynman, R. B. Leighton, and M. Sands, *The Feynman lectures on physics*, New Millenium Edition, Vol. III: Quantum Mechanics (Basic Books, 2010).

[108] F. London, *Superfluids, Macroscopic theory of superconductivity*, Vol. 1, Structure of matter series (Wiley, 1950).

[109] B. S. Deaver and W. M. Fairbank, "Experimental evidence for quantized flux in superconducting cilinders", Phys. Rev. Lett. **7**, 43–46 (1961).

[110] R. Doll and M. Näbauer, "Experimental proof of magnetix flux quantization in a superconducting ring", Phys. Rev. Lett. **7**, 51–52 (1961).

[111] S. Foner, "Versatile and sensitive vibrating-sample magnetometer", Rev. Sci. Instrum. **30**, 548–557 (1959).

[112] R. E. Smallman and A. H. W. Ngan, *Physical metallurgy and advanced materials engineering*, 7th ed. (Butterworth–Heinemann, 2007).

[113] B. Huang et al., "Layer-dependent ferromagnetism in a Van der Waals crystal down to the monolayer limit", Nature **546**, 270–273 (2017).

[114] R. Lavrijsen, J. H. Franken, J. T. Kohlhepp, H. J. M. Swagten, and B. Koopmans, "Controlled domain-wall injection in perpendicularly magnetized strips", Appl. Phys. Lett. **96**, 222502 (2010).

[115] J. H. Franken, M. Hoeijmakers, R. Lavrijsen, and H. J. M. Swagten, "Domain-wall pinning by local control of anisotropy in Pt/Co/Pt strips", J. Phys. Condens. Matter **24**, 024216 (2011).

[116] J. H. Franken, H. J. M. Swagten, and B. Koopmans, "Shift registers based on magnetic domain wall ratchets with perpendicular anisotropy", Nat. Nanotechnol. **7**, 499–503 (2012).

[117] L. Landau and E. Lifshitz, "On the theory of the dispersion of magnetic permeability in ferromagnetic bodies", Phys. Z. Sowjet. **8**, 153–169 (1935).

[118] T. L. Gilbert, "A phenomenological theory of damping in ferromagnetic materials", IEEE Trans. Magn. **40**, 3443–3449 (2004).

[119] M. Farle, "Ferromagnetic resonance of ultrathin metallic layers", Rep. Prog. Phys. **61**, 755–826 (1998).

[120] M. Battiato, K. Carva, and P. M. Oppeneer, "Theory of laser-induced ultrafast superdiffusive spin transport in layered heterostructures", Phys. Rev. B **86**, 024404 (2012).

[121] A. J. Schellekens, K. C. Kuiper, R. R. J. C. de Wit, and B. Koopmans, "Ultrafast spin-transfer torque driven by femtosecond pulsed-laser excitation", Nat. Commun. **5**, 4333 (2014).

[122] J. Seo et al., "Nearly room temperature ferromagnetism in a magnetic metal-rich Van der Waals metal", Sci. Adv. **6**, eaay8912 (2020).

[123] A. Yariv, *Optical electronics*, 4th ed. (Saunders College Pub, 1991).

[124] T. D. Cornelissen, "Optical magnetic switching of ferromagnetic Co/Pt thin films", MSc Thesis (2015).

Appendix A

Size and shape of the laser spot

A.1 Focus and beam size

To achieve both a high resolution and high laser fluence, the spot size of the laser beam should be minimized, meaning the laser beam has to be in focus on the sample. A convenient way of determining the spot size is scanning orthogonal across the interface between the substrate and one of the markers described in section 3.1.

Considering that the thickness of the marker (50nm) is much smaller than the alignment precision of the objective (1µm), the intensity difference of the reflected light across the interface is solely described by a difference in reflectivities R_{sub} and R_{mark}, of the substrate and marker respectively. Furthermore, considering that the spot size (in the order of a few micrometers) is much smaller than the size of the structures (in the order of tens of micrometers), the substrate and marker can be described by two adjoined semi-infinite planes.

The reflectivity along the scanning direction is given by the sum of two heaviside step functions H, given by

$$R(x) = R_{mark}H(x - x_{int}) + R_{sub}H(x_{int} - x), \tag{A.1}$$

where x_{int} is the position of the interface along the scanning axis x.

It is furthermore assumed that the shape of the laser beam is 2-dimensional Gaussian. For a laser beam centered around the z-axis and traveling in the z-direction, the intensity I as a function of spatial coordinates $\boldsymbol{r} = (x, y)$ and z is given by [1]

$$I(\boldsymbol{r}, z) = I_0 \left(\frac{\omega_0}{\omega(z)}\right)^2 \exp\left(\frac{-2|\boldsymbol{r}|^2}{\omega(z)^2}\right), \tag{A.2}$$

where I_0 is the intensity at the center of the beam, $\omega(z)$ is the spot size, which is defined as the $1/e$ beam radius at position z and $\omega_0 = \omega(0)$ is the spot size at the waist of the beam.

[1] Equation A.2 is obtained using the expression for the electric field E given by equation 2.5-14 from Ref. Yariv [123] and inserting this expression into the proportionality $I \propto |E|^2$.

The total power P_R of the reflected signal can now be obtained by multiplying the reflectivity from equation A.1 with a Gaussian beam from equation A.2 centered around a coordinate $\boldsymbol{r_0} = (x_0, y_0)$ and integrating over the entire plane, giving

$$\begin{aligned} P_R &= \int_{-\infty}^{+\infty}\int_{-\infty}^{+\infty} \mathrm{d}x\,\mathrm{d}y\, R(x) I(\boldsymbol{r} - \boldsymbol{r_0}, z) \\ &= \int_{-\infty}^{+\infty}\int_{-\infty}^{+\infty} \mathrm{d}x\,\mathrm{d}y (R_{mark} H(x - x_{int}) + R_{sub} H(x_{int} - x)) \\ &\qquad \times I_0 \left(\frac{\omega_0}{\omega(z)}\right)^2 \exp\left(\frac{-2[(x-x_0)^2 + (y-y_0)^2]}{\omega(z)^2}\right) \\ &= \frac{\pi}{4} I_0 \omega_0^2 \left[R_{mark} + R_{sub} + (R_{mark} - R_{sub}) \operatorname{erf}\left(\frac{\sqrt{2}}{\omega(z)}(x_0 - x_{int})\right)\right]. \end{aligned} \tag{A.3}$$

By scanning the laser beam across the interface, which means varying x_0 in A.3, and measuring the corresponding power of the reflected beam, P_R is obtained as a function of x_0. Fitting equation A.3 through this data subsequently returns the spot size $\omega(z)$. By repeating the process for different focal positions the minimal spot size is obtained for optimal focus.

A.2 Influence of spot size and shape on demagnetization

The amount of demagnetization as determined by measuring hysteresis loops before and after arrival of the pump pulse should be corrected for the Gaussian shape of the pump and probe laser beam. Due to its Gaussian shape, the pump pulse does not induce an equal amount of demagnetization throughout the pumped region, rather the amount of demagnetization is maximum at the center of the beam and decreases with distance from this center. Equivalently, the probe beam is most sensitive to the MOKE signal at the center of the probe spot and reduces as the distance from the center increases.

The maximum amount of demagnetization can be calculated from the demagnetization profile following an approach similar to that in [124], using the following assumptions. First, the low fluence limit is assumed, for which the amount of demagnetization scales linearly with the pulse energy at a certain position. Second, since demagnetization is a much faster process than heat diffusion, the latter is neglected, which means that the excited Gaussian profile will remain constant over time. The magnetization in the pumped region can now be expressed as

$$m(x, y) = 1 - \Delta m_{max} \exp\left(-\frac{x^2}{2\sigma_{pu,x}^2} - \frac{y^2}{2\sigma_{pu,y}^2}\right), \tag{A.4}$$

with $m(x, y)$ the normalized magnetization at spatial coordinates x and y, $\Delta m_{max} = m(0, 0)$ the normalized amount of demagnetization at the center

of the spot and $\sigma_{pu,x}$ and $\sigma_{pu,y}$ the $1/e^2$ spot size in the x and y direction, respectively.

It is furthermore assumed that the pump and probe spot overlap perfectly, which can be approximated in practice by maximizing the second lock-in signal at a certain time delay. It is also assumed that the measured magnetization at some position scales linearly with the probe intensity at that position. As follows, the observed magnetization m_o is expressed as

$$\begin{aligned} m_o &= \frac{\int_{-\infty}^{\infty}\int_{-\infty}^{\infty} m(x,y)\exp\left(-\frac{x^2}{2\sigma_{pr,x}^2}-\frac{y^2}{2\sigma_{pr,y}^2}\right)\mathrm{d}x\mathrm{d}y}{2\pi\sigma_{pr,x}\sigma_{pr,y}} \\ &= 1-\Delta m_{max}\frac{\sigma_{pu,x}\sigma_{pu,y}}{\sqrt{(\sigma_{pr,x}^2+\sigma_{pu,x}^2)(\sigma_{pr,y}^2+\sigma_{pu,y}^2)}}, \end{aligned} \tag{A.5}$$

with $\sigma_{pu,x}$ and $\sigma_{pu,y}$ the $1/e^2$ probe spot size in the x and y direction, respectively.

Lastly, it is used that the second lock-in does not extract the magnetization of the material, but rather the demagnetization $\Delta m_o = 1 - m_o$, yielding

$$\frac{\Delta m_o}{\Delta m_{max}} = \frac{\sigma_{pu,x}\sigma_{pu,y}}{\sqrt{(\sigma_{pr,x}^2+\sigma_{pu,x}^2)(\sigma_{pr,y}^2+\sigma_{pu,y}^2)}}, \tag{A.6}$$

which can be used to determine the maximum amount of magnetization Δm_{max} from the relevant spot sizes and Δm_o, which can be determined by measuring the earlier discussed hysteresis loops.

Appendix B

Elaboration on experimental methods

This section will elaborate on some specific details regarding the used equipment and lists the relevant components used.

B.1 Femtosecond laser system

A train of laser pulses is generated using a mode-locked Ti:sapphire oscillator, which is pumped by a continuous wave, frequency-doubled Nd:YVO_4 laser that has an output power of 4.5W. The output wavelength of the oscillator can be tuned between $720 - 850$nm, the pulse length is $\sim 70 - 80$fs, with a pulse repetition rate of 82MHz and pulse energy of $\sim$ 6nJ. After going through all optical components in the beam path, a stretching of the pulse length towards ~ 100 fs is expected. A spectrometer is used to determine the wavelength of the pulses and a scanning autocorrelator is used for measuring the pulse length. Specific component information is listed in Table B.1.

B.2 Cryostat

A sample-in-vacuum cryostat is used to cool down FGT below its Curie temperature. The cryostat has optical access and is surrounded by two freely rotatable electromagnetic coils in the Helmholtz configuration. Liquid nitrogen is used as a cryogen to cool down and is transferred through a low loss transfer tube from a 100 L vessel. The sample space is pumped down by a turbomolecular vacuum

Table B.1: Laser related components.

Component	Type
Pump laser	Spectra Physics Millenia V
Oscillator	Spectra Physics Tsunami model 3960
Spectrometer	Ocean Optics 2000
Autocorrelator	Light Conversion Geco Scanning Autocorrelator
Lock-in amplifier	Stanford Systems SR830

Table B.2: Cryostat related components.

Component	Type
Cryostat	Oxford Instruments MicrostatHe
Temperature controller	Oxford Instruments ITC503S
Cryogen Flow controller	Oxford Instruments VC31

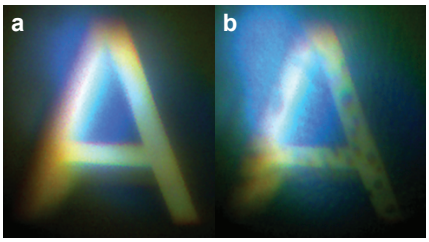

Figure B.1: A photo of (a) an uncontaminated gold marker and (b) a marker that is contaminated by ice droplets.

pump, which is backed by a rotary pump. Specific component information is listed in Table B.2.

During operation, certain steps should be taken to avoid contamination of the sample vacuum space. First, the system should be free of leaks to prevent deposition of ice droplets on the sample. Figure B.1a-b shows a comparison between an (a) uncontaminated golden marker and (b) marker contaminated with ice droplets due to a leak of the cryostat. Since FGT is vulnerable to oxidation, these droplets will oxidize the FGT surfaces and render the samples useless.

Second, a cooled down cryostat will act as a vacuum pump due to cryo-pumping effects and has a generally larger pumping capacity compared to the turbomolecular pump. Therefore, when operating with liquid helium the pressure relieve valve of the cryostat should be completely closed. Operating with liquid nitrogen is more complicated and it is generally advised to very slightly open the pressure relieve valve. In the setup used for this work, approximately a quarter turn past its free travel proved to be sufficient. If this valve is opened too far, small amounts of oil leaking from the rotary pump can travel towards the vacuum space. This oil will slowly deposit on the cold parts of the cryostat, leading to oil buildup on the sample over time and rendering the sample useless for optical experiments.